Journal of Materials Chemistry C

Accepted Manuscript

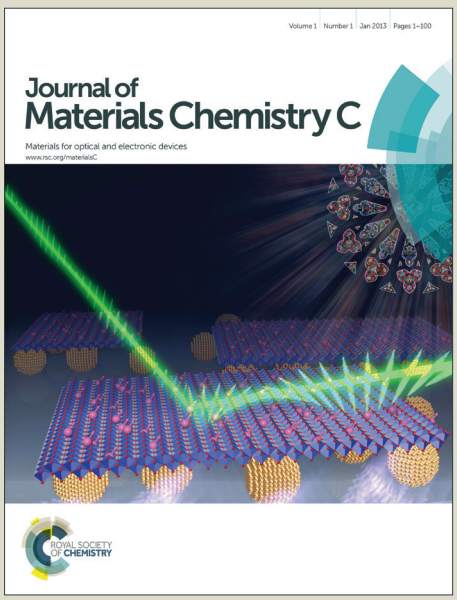

ROYAL SOCIETY OF CHEMISTRY

www.rsc.org/materialsC

Journal Name

RSCPublishing

ARTICLE

Nano-titania doped with europium and neodymium showing simultaneous photoluminescent and photocatalytic behaviour

D.M. Tobaldi,[*a] R.A.S. Ferreira,[b] R.C. Pullar,[a] M.P. Seabra,[a] L.D. Carlos[b] and J.A. Labrincha[a]

Cite this: DOI: 10.1039/x0xx00000x

Received 00th January 2012,
Accepted 00th January 2012

DOI: 10.1039/x0xx00000x

www.rsc.org/

Titanium dioxide (TiO_2) nanomaterials are attracting increasing interest, mostly because of their superior photocatalytic and antibacterial properties. In this work, we report the synthesis, by a "green" aqueous sol-gel route, of TiO_2 doped with Eu and Nd (1 and 5 mol%), in order to extend its photocatalytic activity into the visible range, and also take advantage of the luminescent features of the rare earth metals (REs). Gels were dried in an oven at 75 °C, and then thermally treated at 450 °C in a static air flow furnace. Semi-quantitative phase composition (QPA) and microstructure (crystalline domain shape and size distribution) of the synthetic powders were studied by means of advanced X-ray methods: Rietveld refinements, and the whole powder pattern modelling (WPPM) technique, respectively. From these X-ray techniques, it was seen that the unit cell volume of RE-modified titania underwent a huge expansion, thus suggesting the incorporation of RE into the TiO_2 lattice, accompanied by a decrease in the average crystalline domain diameters of anatase, rutile and brookite. The optical properties were also investigated, by diffuse reflectance spectroscopy (DRS). Photoluminescent behaviour was assessed in the visible and near infra-red (NIR) spectral ranges. Photocatalytic activity of the samples was assessed both in liquid-solid and in gas-solid phase. The influence of the lighting conditions (UV- and visible-light exposure) was also taken into account for evaluating the photocatalytic activity. Nd-TiO_2 was shown to be a bifunctional material, having both photocatalytic activity and NIR photoluminescent emission induced by the same excitation source, an unprecedented result.

Introduction

Semiconductor photocatalysis are one of the most promising technologies to confront the ever-increasing problems of environmental pollution, energy production and emerging penicillin-resistant bacteria.[1,2] Titanium dioxide (TiO_2) is by far the most investigated semiconductor for various applications, such as treating waste-waters[3] and indoor air pollutants,[4,5] photo-splitting of water to produce hydrogen,[6] electrochemical electrodes,[7] solar cells,[8] and antimicrobial agents[9,10] against many bacterial strains[11] and yeasts.[12]

TiO_2 is able to mineralise a wide range of organic and inorganic pollutants, and poisonous materials, both in liquid-solid and gas-solid phases.[13] However, being a wide energy band gap (E_g) material (anatase E_g = 3.2 eV; rutile E_g = 3.0 eV),[14] it is activated only by ultraviolet light, which is only 3-5% of the solar light spectrum.[15] There are several ways of extending TiO_2 light absorption into the visible-light range, such as anionic doping,[16,17] transition metal doping,[18] noble-metal modification,[19–21] or by adopting new strategies such as making hybrid photocatalysts,[22–24] coupling semiconductors for solar light-driven thermocatalysis,[25,26] or preparing upconversion photocatalysts.[27] However, rare earth (RE) doping is becoming increasingly in-vogue and cutting-edge,[28–33] despite the fact that the initial work dealing with REs and TiO_2 goes back as far as 1998.[34] This is because the addition of REs into the TiO_2 lattice might give titania multiple benefits. Due to the transitions of RE 4*f* electrons, the optical absorption of titania is increased, thus moving it into the visible-light range, while also promoting photo-generated electron–hole (e^-–h^+) pair separation.[35] Moreover, modification of a semiconductor with RE^{3+} ions can give the modified material not only luminescent properties, that will show up-conversion luminescence,[36] but also unique optical properties, so prospective applications in optoelectronic devices and biosensors are expected.[37–39] Furthermore, as TiO_2 is a non-

toxic material, the synthesis of nanocrystalline luminescent titania activated with RE ions could be of interest for applications in a number of optical and biotechnological areas, *i.e.* multiplexed labelling, signalling, bioassays, or biomedical purposes, even as a potential drug for killing cancer cells.[40]

Amongst the available literature on RE-TiO_2, many papers deal with the photocatalytic activity (PCA) – both in liquid-solid phase against organic dyes, and in gas-solid phase degrading NO_x or volatile organic compounds (VOCs) – without taking into account the luminescent properties.[30,31,41–46] *Vice-versa*, papers dealing mainly with RE-TiO_2 luminescence properties neglect the photocatalysis side.[47–52] Just recently, the Zaleska group combined both photocatalysis and photoluminescence in RE-doped (and co-doped) titania, showing that RE addition gave titania superior PCA (for phenol and acetic acid oxidation in liquid-solid phase), and also photoluminescent emission (with Er- and Er/Yb-TiO_2).[32,33]

Moreover, the quest for sophisticated multifunctional materials displaying various coexisting properties, *e.g.*, magnetism, catalysis, electrical conduction, and luminescence, is one of the most exciting topics in materials science.[53] One of the most followed approaches for the design of multifunctional materials involves judicious selection of molecular building blocks, each of which imparts a desired chemical or physical property.[54] For instance, magnetism has been combined with luminescence in unique examples of bifunctional molecular materials,[55,56] including single-ion magnets based on Dy^{3+}.[57] Another rational approach for such design is to choose a nanostructure with a specific functionality, and combine it with an ion or other nanostructure with some other functionality.

In this work, our approach was to create a multifunctional material by combining the well-known photocatalytic property of TiO_2 with the luminescent properties of lanthanide ions (Eu^{3+} and Nd^{3+}). In particular, we show that doping TiO_2 with Nd^{3+} gave rise to a bifunctional material, exhibiting simultaneous PCA and NIR photoluminescent emission induced by the same excitation source, which is an unprecedented result. We synthesised, through two parallel "green" aqueous sol-gel routes,[20,21,58] a set of Eu and Nd (1 and 5 mol%) modified TiO_2, using two different RE sources for each RE used. The gels were thermally treated at 450 °C in a static air flow furnace, and a total of 16 different samples were produced and compared. Semi-quantitative phase analysis (QPA) and microstructure (crystalline domain shape and size distribution) of the synthesised powders were studied by means of advanced X-ray methods: Rietveld refinements, and the whole powder pattern modelling (WPPM) technique. The optical properties were also investigated, by diffuse reflectance spectroscopy (DRS).

Photocatalytic activity of the prepared samples was assessed both in liquid-solid and in gas-solid phase – monitoring the degradation of an organic dye (methylene blue (MB)), and nitrogen oxides (NO_x, *i.e.* NO plus NO_2), respectively. The influence of the lighting conditions (UV- and visible-light exposure) was also taken into account for evaluating the photocatalytic activity. Photoluminescent behaviour was assessed in the visible and near infra-red (NIR) spectral ranges. The Eu^{3+} and Nd^{3+} emission spectra are used to discuss the presence of multiple RE^{3+} sites in the TiO_2 phases. Although this discussion has previously been reported for Eu^{3+}-doped TiO_2 crystals,[59] evidence of Nd^{3+} multiple site coordination in TiO_2 phases is presented here for the first time. The Nd^{3+}-doped TiO_2 was shown to be a multifunctional material, having simultaneous photocatalytic activity and NIR photoluminescent emission, induced by the same excitation source.

Experimental

Sample preparation

Aqueous titanium(IV)hydroxide sols were made via the controlled hydrolysis of titanium(IV)isopropoxide (Ti-*i*-pr, $Ti(OCH(CH_3)_2)_4$), using distilled water with an acid catalyst diluted in alcohol, added dropwise, as previously reported in detail by these authors.[20,21,58] This green nanosynthesis process was adapted to add one of two REs as a dopant, europium (Eu^{3+}) or neodymium (Nd^{3+}), in two different quantities, 1 mol% or 5 mol%.

Furthermore, two different kinds of RE salt, chlorides and nitrates, were investigated for each RE ion. For neodymium, commercially available salts were used: $Nd(NO_3)_3 \cdot 6H_2O$ (Aldrich, 99.9%) and $NdCl_3 \cdot 6H_2O$ (Aldrich, 99.9%). Europium nitrate and chloride were synthesised from Eu_2O_3 (Aldrich, 99.5%), by dissolving the oxide in a small excess (a few % above stoichiometry) of the relevant concentrated acid. In this work we used HNO_3 (65% conc., PANREAC PA 180 analysis grade) to make $Eu(NO_3)_3$, and HCl (36% Conc., VWR AnalaR NORMAPUR analysis grade) to make $EuCl_3$. In both cases a small amount of water was added to the acid, and the solution heated at 100 ºC / 1 h to fully dissolve the oxide. These solutions were then further diluted to form a 0.25 M solution of the Eu^{3+} salt.

Two different methods of adding the dopant were also investigated, for comparison of any possible effect on the final properties: 1) Coprecipitation (coppt) of the Ti-*i*-pr with a water/acid/alcohol solution also containing the RE salt, incorporating the RE ions into the interior of the sol particles from their initial formation, and 2) Addition of the salt solution directly to the existing aqueous Ti sol after it had already been synthesised (doping). The salt solutions were all made in distilled water at concentrations of 0.25M, and added stoichiometrically to give doping levels of 1 and 5 mol%.

Therefore, two different RE ions (Nd and Eu) were studied, from two different salts (NO_3^- and Cl^-), with two different synthesis routes (coppt and doping), in two different concentrations (1 and 5 mol%), giving a total of 16 different samples to be investigated. All sols were then evaporated to a gel on a rotary evaporator, and further dried in a drying oven at 70 ºC for at least 24 hours. The synthesis process is summarised in figure 1.

Afterwards, dried gels were thermally treated at 450 °C under a static air flow, using a muffle furnace. The heating / cooling rate was 5 °C min^{-1}, with a 2 hour dwell time at the selected temperature of 450 °C. Samples were referred in the

form ***X*%RE_*Y*_dp/co**, where ***X*** = 1 or 5 mol%; **RE** = Eu or Nd; ***Y*** = C or N, referring to the RE salt used (C = Cl^-, N = NO_3^-); and **dp** or **co** stands for doping or coppt, respectively. This is also shown in figure 1.

Sample characterisation

The size distributions of the starting sols were measured *via* photon correlation spectroscopy (PCS) using a Zetasizer Nano ZS (Malvern Instruments, UK). 4 drops of the 1M sol were added to a cuvette of distilled water, and measured at room temperature (RT), after being allowed to stabilise for 10 min. The scattering was measured at an angle of 173º, using a 633 nm laser, and assuming the refractive indexes of water and the $Ti(OH)_4$ based sol particles to be 1.33 and 2.50, respectively. Size information was calculated from the correlation function and cumulants analysis using the CONTIN method. Number size values were obtained from refinements using Mie theory, to reflect the true size distribution. Particle sizes were measured between 0.4 and 10^3 nm.

Semi-quantitative phase analysis (QPA) of the samples was achieved by means of X-ray powder diffraction (XRPD), although from previous works, we know that this nanosynthesis method results in a not-negligible amount of amorphous phase.[20,60] XPRD data were collected using a θ/θ diffractometer, PANalytical X'Pert Pro (NL), equipped with a fast RTMS detector (PIXcel 1D, PANalytical), with Cu Kα radiation (45kV and 40 mA, 20-80 °2θ range, a virtual step scan of 0.02 °2θ and virtual time per step of 100 s). The incident beam pathway was composed of: 0.5° divergence slit, 0.5° anti-scattering slit, 0.04 rad soller slits, and a 15 mm copper mask. The Rietveld method, as implemented in GSAS-EXPGUI software packages,[61,62] was used with the aim of detecting the crystalline phases that are in the samples – *i.e.* not accounting for the likely presence of amorphous phase: semi-quantitative phase composition (QPA). The starting atomic parameters for anatase, rutile and brookite, described in the space groups $I4_1/amd$, $P4_2/mnm$ and *Pbca* respectively, were taken from a previous work by the authors.[60] Instrumental contribution, obtained from the NIST SRM 660b standard (LaB_6), was also estimated in the refinements, and the following parameters were refined: scale-factors, zero-point, six coefficients of the shifted Chebyshev function to fit the background, unit cell parameters, two Lorentzian (L_X and L_Y) terms and one Gaussian term (G_W, an angle independent term) as the profile coefficients, and sample displacement effects.

The microstructure of the synthesised REs-TiO_2 nanoparticles (NPs) was also studied from XRPD data, collected using the same instrument having the same set-up, but, with the aim of handling data having a high signal/noise ratio, these were collected in the 20–125 °2θ range, with a virtual step scan of 0.1 °2θ, and virtual time per step of 500 s. Microstructural features were analysed *via* the whole powder pattern modelling (WPPM) method,[63] through the PM2K software.[64] This novel procedure allows us to extract microstructural information from a diffraction pattern, by refining model parameters *via* a non-linear least squares routine, so as to fit the experimental peaks, without any use of arbitrary analytical functions (*i.e.* Gaussian, Lorentzian, or Voigtian). The diffraction peak profile is actually the result of a convolution of instrumental and sample-related physical effects. This way, the analysis is considered taking into account physical models of microstructure and / or lattice defects.[65,66] Essentially, with the WPPM method, aspects of microstructure such as the crystalline domain shape and size distribution can be truly assessed, with a method significantly superior to the estimations made by other frequently used integral breadth methods for line profile analysis (LPA) – *i.e.* the routinely used Scherrer formula,[67] or the Williamson–Hall method.[68] In fact, using these other methods,[67,68] it can be tricky to correctly extract integral breadths, because of the instrumental profile component, background and peak profile overlapping. Furthermore, additional sources of line broadening – *i.e.* domain size and / or lattice strain – cannot be considered properly by LPA methods.[69] The instrumental contribution was obtained by modelling 14 *hkl* reflections from the NIST SRM 660b standard (LaB_6), according to the Caglioti *et al.* relationship.[70] Afterward, anatase (SG $I4_1/amd$), rutile (SG $P4_2/mnm$) and brookite (SG *Pbca*) were included in the WPPM modelling. The following parameters were refined: background (modelled using a 6^{th}-order of the shifted Chebyshev polynomial function), peak intensities, specimen displacement, and lattice parameters. In this work, crystalline domains were assumed to be spherical, and their diameter distributed according to a lognormal size distribution.

Diffuse reflectance spectroscopy (DRS) was performed using a Shimadzu UV 3100 (JP) spectrometer, equipped with an integrating sphere and a white reference material, both made of $BaSO_4$. Spectra of the samples were acquired in the UV–Vis range (250−750 nm), with 0.2 nm in step size. The Kubelka-Munk function was applied in order to convert the diffuse reflectance into the absorption coefficient α:

$$\alpha \approx \frac{K}{S} = \frac{(1-R_\infty)^2}{2R_\infty} \equiv F(R_\infty) \qquad (1)$$

where K and S are the absorption and scattering coefficients; the reflectance R_∞ is equal to $R_{sample}/R_{standard}$.[71]

The optical E_g of the powders was calculated by using DRS and taking advantage of the differential reflectance method. This method supposes that, plotting the first derivative of reflectance ($dR/d\lambda$) versus the wavelength (λ), the maximum value of such a plot corresponds to the optical E_g of the semiconductor material.[17,72] The resulting curves were fitted adopting a Gaussian function (Origin ProLab, version 8.5.0), and the maximum values were found from the fitting itself.

Raman spectra of selected samples were acquired in the 50-700 cm^{-1} wavelength range, with 2 cm^{-1} resolution, on a RFS 100/S (Bruker, DE) equipped with a Nd:YAG laser (1064 nm) as the excitation source.

High resolution TEM (HR-TEM) analysis was performed using a JEOL 2200FS microscope with a field emission gun, operated at 200 kV. Samples were prepared by dispersing the

NPs in isopropanol, and evaporating the suspension drops on carbon-coated copper grids.

Photocatalytic activity

PCA of the prepared REs-TiO_2 was assessed both in gas- and liquid-solid phase. The latter experiments were attained using only UV-light exposure. This was done because a dye (methylene blue, MB) was used as a model pollutant, and it can be excited by visible-light irradiation. Consequently, such dyes can act as sensitisers, with an electron injection from the photo-excited dye to the photocatalyst.[73,74] Hence, this electron transfer can destroy the regular distribution of conjugated bonds within the dye molecule, and cause its decolourisation, but not its mineralisation, giving a false indication of PCA.[75,76] The photocatalytic tests in liquid-solid phase, were assessed by monitoring the degradation of MB (Aldrich), using a spectrometer (Shimadzu UV 3100, JP). Tests were performed at RT, in a cylindrical photocatalytic reactor (80 mm in diameter) containing an aqueous solution of the dye (0.5 L), at an initial concentration of 5 mg L^{-1}. The concentration of the photocatalyst in the slurry was 0.25 g L^{-1}. To mix the solution thoroughly, the slurry was magnetically stirred throughout the reaction; the reactor was covered with a watch-glass, so as to avoid the evaporation of the solution. The lighting of the reacting system was achieved by placing two UV lamps at either side of the reactor; the distance between the lamps and the reactor was 5 cm. The UV light sources were germicidal lamps (Philips PL-S 9W, NL), with an irradiance of approximately 13 W m^{-2} in the UVA range – measured with a radiometer (Delta OHM, HD2302.0, IT) – the emission spectrum of the lamps used being reported in Fig. S1a. In the experiments, the photocatalytic degradation of MB was monitored by sampling about 4 mL of the slurry from the reactor, at regular time intervals. Before switching the lamps on, the suspension was stirred in the dark for 30 min, with the aim of allowing the adsorption / desorption of MB onto the powder. The powder in the samples were separated by centrifugation, and then the MB concentration in the liquid was determined, taking advantage of the Lambert-Beer law, by measuring the absorbance in a spectrometer at a wavelength of 665 nm, using distilled water as a reference. The extent of MB photocatalytic degradation ξ was evaluated as:

$$\xi\% = \frac{C_0 - C_S}{C_0} \times 100 \qquad (2)$$

where C_0 is the initial MB concentration and C_S is the concentration after a certain UV irradiation time. Control experiments, to detect likely photolysis of the MB dye under direct UV-light irradiation, were performed prior to testing the PCA of the prepared samples. This was considered negligible, the ξ value being equal to ~3% after 7 h of UV-light irradiation time.

Gas-solid phase. The reactor employed for gas-solid phase tests, operating in continuous conditions as previously described in detail,[21,58,77] is made of a 35 L stainless steel cylinder. Its top was sealed and covered with a glass window, to allow the light to reach the photocatalyst placed inside it. The light sources employed were a solar lamp (Osram Ultra-Vitalux, 300 W) – re-creating an outdoor situation – and a white light irradiating only in the visible region (Philips LED Bulb Warm white)[78] – hence simulating artificial indoor lighting. Emission spectra of the lamps used are shown in Fig. S1b,c†. For the solar lamp, the distance between it and the photocatalyst was 85 cm. The light intensity reaching the samples, measured with a radiometer (Delta OHM, HD2302.0, IT), was found to be approximately 3.6 W m^{-2} in the UVA range, and 25 W m^{-2} in the visible-light range. The white LED lamp was placed 28 cm from the photocatalyst, so as to have a light intensity reaching it of about 7 W m^{-2} in the visible range, and being zero in the UVA.

Samples were prepared in the form of a thin layer of powder, with a constant mass (~0.10 g), and thus approximately constant thickness, in a 6 cm diameter Petri dish (irradiated surface *ca.* 28.3 cm^2). The tests were performed at 27±1 °C (temperature inside the reactor) with a relative humidity of 31%. These parameters – controlled by means of a thermocouple that was placed inside the chamber, and a humidity sensor placed in the inlet pipe – were stable throughout the tests. The outlet concentration of the pollutant gas was measured using a chemiluminescence analyser (AC-30 M, Environment SA, FR). After having placed the photocatalyst inside the reactor, and covered the glass window, the inlet gas mixture (prepared using synthetic air and NO_x gas) was allowed to start flowing until it stabilised at a concentration of 0.2 ppmv – consistent with ordinary indoor concentration.[79,80] Two mass flow controllers were used to prepare such a mixture of air with this concentration of NO_x, and with a flow rate of 1 L min^{-1}. This step was necessary to guarantee the sample saturation, assuring that during the test any measurement of NO_x is solely due to the photocatalytic process – *i.e.* no absorption from the sample, nor from the reactor walls).[81] Once the desired concentration of 0.2 ppmv was attained, the window glass was uncovered, the lamp turned on, and the PCA reaction started. The photocatalytic reaction was reckoned to be completed when the pollutant concentration reached a minimum and stable level, and the sample could no longer keep on decomposing any NO_x.

The photocatalytic efficiency was evaluated as the ratio of the removed concentration of NO_x. The conversion rate (%) of the initial NO_x concentration was calculated as:

$$NO_x conversion\% = \frac{(NO_x)_0 - (NO_x)_S}{(NO_x)_0} \times 100 \qquad (3)$$

where $(NO_x)_0$ and $(NO_x)_S$ are, respectively, the initial NO_x and the NO_x concentration (both expressed as ppmv) after a certain irradiation time.[82] Moreover, with the aim of having a better comparison between the tested samples, data relative to the first

20 min of reaction time were elaborated according to a first order kinetic law. Photocatalytic tests of selected samples were repeated in triplicate, using the very same sample and with the same protocol of the first test, aiming at checking the repeatability, recyclability and photostability of the prepared photocatalysts.

Photoluminescence spectroscopy

The photoluminescence spectra in the visible and NIR spectral ranges were recorded at room temperature with a modular double grating excitation spectrofluorimeter with a TRIAX 320 emission monochromator (Fluorolog-3, Horiba Scientific) coupled to a R928 and H9170 Hamamatsu photomultipliers, respectively, using the front face acquisition mode. The excitation source was a 450 W Xe arc lamp. The emission spectra were corrected for detection and optical spectral response of the spectrofluorimeter and the excitation spectra were corrected for the spectral distribution of the lamp intensity using a photodiode reference detector.

Results and discussion

Sol preparation and characterisation

The synthesis and behaviour of the RE-TiO_2 sols was generally similar to that of the undoped TiO_2 sols made with nitrate and chloride counter ions, as reported by the authors previously.[20,58] The synthesis of the nitrate and chloride based TiO_2 sols, for subsequent doping with RE salts, was exactly as reported previously. With nitrates, the initial hydrolysis passes through a gelatinous phase during precipitation to give a milky white mixture, which evaporates to a jelly-like mass. When this is dispersed in water, it dries to a jelly-like mass again, but this now disperses almost instantly in water to form a bluish-white sol. With chlorides, a thixotropic viscous gel results after hydrolysis (more linking between particles), which evaporates to give a very gelatinous solid. This is dispersed in water and dries to a fine, viscous gel, which disperses almost instantly in water to form a yellowish off-white sol, indicating a smaller particle size than that formed with the nitrates. In these pure TiO_2 sols, the nitrate based route indeed gave slightly larger sol particles than the chloride route (3.61 versus 2.20 nm No. av, respectively), and the nitrates also gave a wider size range (2-10 nm versus 1.5-5.6 nm, respectively).[58]

The particle sizes of the RE-TiO_2 sols were analysed by PCS, using the number average (No. av) size distribution, as this gives an accurate reflection of the actual sizes of the sol particles. The results are given in Table 1. It can immediately be seen that while the Nd-TiO_2 sols all still have small No. av values <8 nm and upper size limits no greater than 20 nm, the Eu-TiO_2 sols mostly have larger values, especially the nitrate-based systems, with No. av up to 50 nm and upper limits of >100 nm. Addition of $Nd(NO_3)_3$ or $NdCl_3$ solutions had no apparent effect upon sol stability, and only a slight increase in sol particle size was observed. There was also little difference between the coprecipitation or doping methods, with coprecipitation resulting in only slightly smaller particles. The uniformly low standard deviation values demonstrated the highly monodisperse nature of these sols.

Coprecipitation with $EuCl_3$ (**1%Eu_C_co** & **5%Eu_C_co**) also led to sols with small No. av and upper limits, similar to those of the Nd-TiO_2 sols. These formed an extremely dense and thixotropic precipitate upon hydrolysis, probably due to extra chloride ions from the $EuCl_3$, which evaporated to a crusty white gel. On dispersal in water and drying they formed a dense, crystalline-looking gel, which immediately dispersed to a white sol. However, doping of the chloride TiO_2 sol with $EuCl_3$ (**1%Eu_C_dp** & **5%Eu_C_dp**) gave sols with larger No. av of ~14 nm, and upper limits of 30-40 nm, so the addition of this salt to a preformed sol reduces its stability and causes sol particle growth. $Eu(NO_3)_3$ seemed to have a much more harmful effect on the sols, with both doped and coprecipitated samples showing much larger No. av of 32-50 nm and upper limits of 80-125 nm, with much greater standard deviations also reflecting the broader distribution of particle sizes. With coprecipitation (**1%Eu_N_co** & **5%Eu_N_co**), the solid formed after evaporation of the solid was much less gelatinous than normally observed with nitrates, and this dried to a very hard glassy gel. Despite this, it dispersed in water to form a sol very easily, but after standing overnight, a small amount of sediment was observed at the bottom of the sol, which will consist of the larger >100 nm particles. When the $Eu(NO_3)_3$ solution was added to existing TiO_2 nitrate sols (**1%Eu_N_dp** & **5%Eu_N_dp**), although they appeared stable at first, a small amount of solid was also found in **5%Eu-N-dp** after standing overnight, and this sol also had the largest No. av of ~51 nm and upper limit of 125 nm.

Therefore, it seems that all of the RE-TiO_2 sols were stable systems except for those based on europium nitrate, $Eu(NO_3)_3$. All further characterisation and measurements were carried out on the powders after firing at 450 ºC.

X-ray diffraction analysis

Quantitative phase analysis. XRPD data are shown in Table 2; an example of a Rietveld refinement is depicted in Fig. S2†. All the XRD patterns show the presence of reflections belonging only to TiO_2 oxides (anatase, rutile and brookite, though in different amounts, according to the RE added, and to the preparation method). There is no evidence of any RE-titanate, nor RE^{3+} oxide − as also confirmed by Raman spectra (*cf* **Fig. 2**) − probably indicating a solid solution between TiO_2 and RE_2O_3 (*cf microstructural analysis* section).

The undoped TiO_2, when heated to 450 ºC, was composed of 42.9 wt% anatase, 49.1 wt% rutile, and 8.0 wt% brookite. RE addition heavily favoured brookite crystallisation (proportional to mol% RE), compared to the undoped TiO_2, which is consistent with previous reports on Eu- and Nd-TiO_2.[83–85] This was also accompanied by a lower amount of rutile in the RE modified samples. Brookite wt% in the samples ranged from 30.5 wt% for **1%Eu_N_co** to 57.3 wt% for **5%Eu_N_dp**, and made up between $^1/_3$ to ½ of all the other samples.

The presence of brookite is to be expected, as it is a common (by-)product of such sol-gel syntheses,[86–88] together with anatase, the latter being the more thermodynamically stable TiO_2 polymorph at the nanoscale.[89] Also, the pH of the pure TiO_2 sols is already highly acidic (pH ~ 1), which favours brookite crystallisation.[90,91,86] The addition of RE salts, effectively creating HNO_3 or HCl, increased the acidity of the sols even more up to a pH ~0.2, thus favouring greatly brookite crystallisation, resulting in such large quantities of it, and this apparently occurred at the expense of rutile (*cf* Table 2). In fact, brookite crystallisation is reported to follow a dissolution–precipitation process that is significantly promoted in a highly acidic environment,[92] and its transition to rutile is reported to happen in the 500−600 °C temperature range.[93]

In particular, we found that with Eu, using nitrate salts (**1%Eu_N_dp**, **1%Eu_N_co**) and the co-precipitation method (**1%Eu_C_co**) both favoured more rutile formation, compared to the Nd-doped sols. Using $EuCl_3$, on the other hand, gave more anatase, particularly in the coprecipitated sols (**5%Eu_C_co**). Therefore, the least stable sol systems also favoured rutile formation upon heating, and the Eu-TiO_2 sols with the smallest particles sizes favoured production of more anatase. With Nd addition, there was a little difference in the phase composition when nitrates were used, with either doping or co-precipitation, and anatase was strongly favoured (**1%Nd_N_dp**, **1%Nd_n_dp**). When using $NdCl_3$, however, anatase content decreased slightly, with a higher amount of brookite. In general, the Nd-TiO_2 sols, which had less variation in sol particle size than the Eu-TiO_2 sols, also had less variation in phase composition, and favoured anatase over rutile.

MICROSTRUCTURAL ANALYSIS. Unit cell parameters, as calculated *via* the WPPM method, are shown in Table 3; an example of the WPPM graphic output for sample **1%Eu_N_dp** is depicted in Fig. S3†. For anatase, it was seen that both unit cell parameters *a* and *c*, and unit cell volume, of the samples modified with both REs are all greater than those of the unmodified TiO_2. The unit cell volume expansion had a linear relation with the mol% RE added. This trend was also observed, though to a lesser extent, in rutile, but only when doped with neodymium. The RE ion seems to have been accommodated preferentially along the *a*-axis, this being longer in the modified samples. Concerning brookite, in general its unit cell parameters (and unit cell volume, as a consequence), do not vary significantly in the RE modified samples, compared to the undoped TiO_2, and are within the experimental error.

Therefore, based on this, and according to Vegard's law, the incorporation of Eu^{3+} and Nd^{3+}into the anatase lattice (and to a lesser extent the rutile lattice, in case of Nd^{3+}) can be hypothesised, despite the large mismatch in both charge and ionic radii (effective ionic radius of $^{[VI]}Ti^{4+}$ = 0.605 Å, $^{[VI]}Eu^{3+}$ = 0.947 Å, $^{[VI]}Nd^{3+}$ = 0.983 Å).[94] However, although often considered unusual, this behaviour has already been reported.[59,95,96] Luo *et al.*, using a sol-gel solvothermal method, incorporated Eu^{3+} into the anatase lattice, and they demonstrated this with extended X-ray absorption of fine structure (EXAFS) and photoluminescence data.[59] Ghigna *et al.*, by means of a sol-gel synthesis method, also showed with EXAFS and photoluminescence measurements that Nd^{3+} entered the anatase structure as substitutional defects with respect to Ti. This was accompanied by a huge increase in disorder around those defects,[95] as also confirmed by Raman analyses, *cf* **Fig. 2**, and Table 4. **In the inset of Fig. 2**, and Table 4, it is actually shown that the E_g Raman mode of anatase (at around 144 cm^{-1}) in the RE-TiO_2 underwent a red-shift, compared to the undoped titania, whilst its full width at half maximum (FWHM) increased. This corroborates the afore-mentioned hypothesis of increased disorder, owing to RE-doping, in TiO_2 structure.[97,98] In both the cases, the authors did not report any evidence of Eu_2O_3 or Nd_2O_3 segregation around titania NPs. Moreover, in the anatase lattice, Ti^{4+} is accommodated in D_{2d} symmetry, with four short Ti−O (basal) and two long Ti−O (apical) bond lengths (the average Ti−O bond length being around 1.95 Å). The average Eu−O and Nd−O bond lengths are 2.32 and 2.47 Å, respectively.[59,95] Thus, they are 0.37 and 0.52 Å, respectively, longer than the Ti−O average bond distance. This difference can be readily fulfilled by the difference in ionic radii between RE^{3+} and Ti^{4+} having coordination number = VI (the difference in ionic radii is 0.342 and 0.378 Å, for Eu^{3+}/Ti^{4+} and Nd^{3+}/Ti^{4+}, respectively). Nd substitution of Ti in rutile has already been described by Le Boulbar *et al.*, who obtained various Nd^{3+}doping levels of 1, 2 and 5 mol%.[99] Moreover, Bouras and co-workers recently found Nd^{3+} substitutional incorporation in SnO_2, which is isostructural with rutile, synthesised *via* a sol-gel method and thermally treated at 700 °C.[100] Ti^{4+} in rutile has a D_{2h} symmetry,[101] with four basal Ti−O and two apical Ti−O bond lengths, and as in anatase, the average Ti−O bond length is ~1.96 Å.[60] Hence we can make the same considerations as for anatase regarding RE incorporation into the rutile structure.

Average crystalline domain size and the log-normal size distribution of anatase, rutile and brookite in the samples, as inferred from XRPD *via* the WPPM method, are depicted in Table 5 and Fig. S4†. The information obtained on the NP's crystalline domain size shows that, in the unmodified sample, anatase, rutile and brookite had average diameters of 8.6, 17.7 and 11.2 nm, respectively. Brookite had the narrower size distribution, its mode being 10.6 nm; rutile, on the contrary, had the widest size distribution, the mode being 13.8 nm. Generally speaking, addition of Eu^{3+} and Nd^{3+} led to a huge decrease of anatase, rutile, and brookite average crystalline domain diameters, compared to the undoped TiO_2. This finding was confirmed by HR-TEM analysis (**Fig. 3a-c**). The large degree of agglomeration of the NPs can also be seen from HR-TEM microgarphs. Overall, in the RE-TiO_2 the average anatase NP domain diameters were all similar, at about 6 nm, and with a narrower size distribution compared with anatase in undoped titania. For rutile, the decrease in the average crystalline domain diameter followed the amount of RE added: the higher the RE amount, the lower the average NP domain diameters (with sizes ranging from 6.6-13.2 nm). Brookite experienced the greatest reduction in size, which with REs was approximately half than of the unmodified TiO_2 (average

diameters ranging from 3.7-7.0 nm). Also in this case, the higher the amount of RE added, the lower the average domain diameter, which also had a narrow size distribution. This behaviour is consistent with the large amount of brookite found in the RE-TiO_2 samples, due to the arrested brookite-to-rutile phase transformation, which is a nucleation and growth process.[93] In general, it can be said that the RE−O−Ti bonds formed may restrain the crystallisation processes of TiO_2, hence suppressing crystalline domain growth in the NPs.[102]

Optical properties

Optical data are reported in Fig. 4a,b and Table 6. All the DRS spectra show, at around 400 nm, the metal-ligand charge transfer (MLCT) absorption band in titania [103] – RE doping did not significantly (red) shift the main absorption band edge of titania. Moreover, DRS spectra of RE-TiO_2 with the same RE (Eu^{3+} or Nd^{3+}) at the same concentration are all virtually identical. Hence, here we will only describe those with the higher amount (5 wt%) of each RE, as the intensity of RE absorption bands decrease with their molar content in titania. In the spectra of 5 mol% Eu-TiO_2 (**5%Eu**, Fig. 4a), the presence of two small sharp peaks at 465 nm (2.67 eV) and 532 nm (2.33 eV) is noticeable. They are respectively assignable to the Eu^{3+} 4*f* transitions $^7F_0 \rightarrow {}^5D_2$ and $^7F_0 \rightarrow {}^5D_1$.[104] The Nd-$TiO_2$ spectra (**5%Nd**, Fig. 4b) are also characterised by the presence, in the range 400-750 nm, of transitions between the ground-state $^4I_{9/2}$ and the excited states within the Nd^{3+} 4*f* shell.[105] In particular, the most intense band, centred around 586 nm (2.12 eV), is assignable to the transitions from the ground state, $^4I_{9/2}$, to the excited states $^4G_{5/2}$ and $^2G_{7/2}$. The absorption band centred at around 528 nm (2.35 eV) is due to transitions between the ground state $^4I_{9/2}$, and the $^4G_{7/2}$, $^4G_{9/2}$, and $^2K_{13/2}$ states, whilst the band at around 684 nm (1.81 eV) can be ascribed to $^4F_{7/2}$ and $^4S_{3/2}$ transitions.[106–108]

As per the apparent optical E_g, their values were estimated by means of the differential reflectance method, and are reported in Table 6. The main peak, having a maximum value at around 405 nm (3.06 eV), was assigned to the rutile optical E_g, and this was detected in all the samples. In the undoped TiO_2, this had a value of 3.06 eV (405 nm), which is consistent with the its expected E_g value (3.02 eV; 411 nm).[14] The rutile E_g in the RE-TiO_2 is equal to, or blue-shifted compared to, that of rutile in the undoped TiO_2, with values ranging from 3.06-3.11 eV (405-399 nm), *cf* Table 6. This blue-shifting can probably be attributed to the higher amount of amorphous phase in these samples, rather than to a quantum-size effect.[109]

With regard to the anatase optical E_g, where estimated, this ranged from 3.17-3.32 eV (391-373 nm). Such values are around that expected for anatase, which is reported to be 3.23 eV (384 nm).[110]

The peak at around 3.40 eV (365 nm), *cf* Fig. S5† – found mainly in the 5 mol% RE-doped samples (hence, in those samples with the highest amount of brookite) − was assigned to the optical E_g of brookite.[111,112] Actually, for the sake of clarity, many literature data about brookite E_g are conflicting, with reported values ranging from 3.1-3.4 eV (*i.e.* 400-365 nm) being reported by the scientific community. There is still no agreement or consensus on whether the optical response is attributable to direct or indirect transitions.[113] However, the 3.40 eV (365 nm) value found here is consistent with that determined by Koelsch *et al*. in brookite NPs, and obtained *via* the optical transmission of brookite dispersions at different concentrations, estimated by UV fluorescence measurements.[111]

All in all, the optical E_g did not exhibit a significant lowering in the doped samples – on the contrary, it slightly blue-shifted. This is consistent with what already reported in the literature, and it was attributed to the movement of the conduction band of TiO_2 above the first excited state of RE^{3+}. As a matter of fact, RE^{3+} ions at the first excited state interact with the electrons of the conduction band of TiO_2, resulting in a higher energy transfer from the TiO_2 to RE^{3+} ions.[97,114,115]

Photoluminescence spectroscopy

Fig. 5a shows the NIR emission spectra of selected Nd^{3+}-doped materials. The spectra are formed of the $^4F_{3/2} \rightarrow {}^4I_{9/2\text{-}13/2}$ intra-$4f^3$ transitions. The energy, number of Stark components and FWHM strongly depend on the excitation wavelength. In particular, the FWHM under direct intra-$4f^3$ excitation (586 nm, Fig. 5a) is larger than that observed under lower excitation wavelengths (*e.g.* 350 nm, Fig. 5a), revealing a maximum intensity peak position at 1090 nm and 1070 nm, respectively, with FWHM values around 7 and 20 nm. This readily points out the presence of, at least, two distinct Nd^{3+} average local coordination sites, labelled hereafter as **Site 1** and **Site 2**. The lower relative value of the FWHM for **Site 1** suggests more crystalline Nd^{3+} surroundings, compared with those found in **Site 2**. The presence of more than one Nd^{3+} local-site is further supported by the dependence of the excitation spectra on the monitoring wavelength. The spectra monitored at 1090 nm (**Site 1**) reveal the presence of a series of intra-$4f^3$ lines, overlapping a higher-relative intensity band centred at 385 nm, ascribed to transitions of the anatase phase, as detailed in the DRS analysis. A shoulder at around 356 nm was attributed to the presence of smaller anatase nanocrystallites (with radii between 0.5 and 2.5 nm), located in the amorphous titania walls,[116] or due to the presence of defects assigned to unsaturated titanium ions at the crystal surface, or at the interface between the nanocrystallite and the amorphous matrix.[117] The contribution of the anatase phase for the excitation spectra monitored around 1090 nm indicated that the Nd^{3+} ions in **Site 1** entered the anatase lattice, an efficient host-to-Nd^{3+} energy transfer being observed, as pointed out by the higher relative intensity of the anatase band compared with that of the intra-$4f^3$ lines. Analogous energy transfer was also observed in other Eu^{3+}-doped TiO_2 nancrystals.[59,116] The spectra monitored at 1070 nm (**Site 2**) reveals a significant increase in the relative intensity of the intra-$4f^3$ lines, with respect to the anatase-related components. The contribution of

the anatase phase in the excitation spectra monitored within 1070 nm arises due to the overlap between the emissions arising from **Site 1** and **Site 2**, which disable a selective monitoring of the excitation path for each local coordination site. Nevertheless, the lower contribution of the anatase phase for the excitation spectra preferentially monitored within **Site 2**, and the favouring of the direct intra-4f^3 excitation, is in good agreement with the incorporation of the Nd^{3+} ions in rutile, although to a much lesser extent compared with that observed in anatase.

Fig. 6a shows the emission spectra of selected Eu^{3+}-containing materials. The spectra are formed of the $^5D_0 \rightarrow {}^7F_{0\text{-}4}$ transitions, whose energy and FWHM is independent of the excitation wavelength (Fig. S6†), unlike that found for the Nd^{3+}-based compounds (Fig. 5). The independence of the Eu^{3+} emission spectra to the excitation wavelength suggests that all the ions occupy, on average, the same local environment, as also pointed out by XRD analysis, which revealed Eu^{3+} substitution for Ti^{4+} just in the anatase lattice. We note the broad profile of the intra-4f^6 lines, well-illustrated by the $^5D_0 \rightarrow {}^7F_0$ FWHM value of ~2 nm (~100 cm^{-1}), which indicated the coordination of the Eu^{3+} ions at very disordered sites probably located near the surface of the nanocrystals. Moreover, the maximum Stark splitting of the $^5D_0 \rightarrow {}^7F_1$ transition into 3 components, and the higher relative intensity of the $^5D_0 \rightarrow {}^7F_2$ transition revealed that the Eu^{3+} ions are located in a very low-symmetry local site without an inversion centre, previously ascribed to the lowest site symmetry C_1.[59] The excitation spectra monitored within the $^4D_0 \rightarrow {}^7F_2$ transition (Fig. 6b) display a series of intra-4f^6 transitions, and no sign of the TiO_2 polymorph (anatase) related contribution could be observed. This fact agree well with the coordination of the Eu^{3+} ions to disordered sites near the surface, preventing efficient host-to-Eu^{3+} energy transfer, as already observed Eu^{3+}-doped nanocrystals prepared by sol-gel solvothermal synthesis.[59]

Photocatalytic activity

As liquid–solid and gas–solid phase results are not directly comparable – different target pollutants in a different phase and at different initial concentrations, with different initial amounts of photocatalyst and different lamps used – they will be discussed separately. Literature data also shows that reaction rates in gas-solid phase are different compared to those in liquid-solid phase.[118–120]

Liquid-solid phase. PCA results in liquid-solid phase, only using the UV-lamp, are shown in Fig. S7. These are reported as the apparent pseudo-first order rate constant, k'_{app}. As it is seen in the figure, all the RE-TIO$_2$s are photocatalytically active under these conditions (UV-light irradiation, 7 h total irradiation time, MB degradation). Moreover, the higher the RE amount (regardless of the RE used), the lower the PCA. The higher photocatalytic degradation, amongst the RE-doped samples, was achieved by sample **1%Nd_C_dp** (k'_{app} = 16.9 h^{-1} × 10^2); the lower by sample **5%Nd_C_co** (1.0 h^{-1} × 10^2). However, it is to say that these degradation values are all lower than that obtained with the undoped TiO_2, that reached a k'_{app} value equal to 55.9 h^{-1} × 10^2 – value that is about half than that attained by the reference commercial sample **P25**, that degraded all the organic pollutant in 4 h UV exposure time, and having an apparent pseudo-first order rate constant equal to 117 h^{-1} (datum not reported in Fig. S7). These results are consistent with those achieved by Bettinelli *et al*., whose RE-TiO_2 (RE^{3+} = Er, Eu, Sm), had a PCA (in liquid-solid phase, and degrading MB) lower than that of **P25**. These authors justified that behaviour by a high degree of disorder in the RE-TiO_2 compared to P25, creating different charge transport behaviour (obtained by Monte Carlo simulation) in RE-TiO_2 and P25.[121] Furthermore, the higher PCA of RE-TiO_2 compared to undoped TiO_2 can be attributed to their smaller size, thus giving them higher specific surface area values, and also to a higher amount of hydroxyl radicals adsorbed on their surface, as suggested by Lin and Yu.[34]

Gas-solid phase. PCA results in gas-solid phase, with the solar and the white lamp as light sources, are reported in Fig. 7a,b. Unlike the liquid-solid phase, there was no observed general trend in the gas-solid phase PCA experiments (*cf* previous section, *Liquid-solid phase*). When using a lamp simulating the full solar spectrum (Osram Ultra-Vitalux), all the RE-TiO_2 samples were more active than our unmodified titania, which was the least active sample within the series. **1%Nd_N_co** possessed a PCA even better than **P25**, the commercial reference material, under solar light. Apart from that, all samples exhibited a lower PCA than **P25**. Again, this might be due to different charge transport behaviours in RE-TiO_2 and P25, and/or to the defects induced by RE^{3+} doping, giving rise to recombination centres for the photo-generated couple.[121,122] However, it is interesting to note that that majority of the RE-TiO_2 samples were close to the median PCA value, (shown by the horizontal dashed line in Fig. S8a†). Both $Nd(NO_3)_3$ doped sols (**1%Nd_N_dp** & **5%Nd_N_dp**), **5%Eu_C_co**, and especially **1%Eu_N_dp**, showed poor PCA under solar light.

Very different PCA behaviour was observed using white light. Our unmodified TiO_2 had a PCA virtually identical to **P25**,[58] due to the concomitant presence of anatase and rutile NPs in both these titanias − when nanostructured, rutile is reported to be a visible-light active photocatalyst.[123] Hurum *et al*., using electron paramagnetic resonance (EPR) spectroscopy, showed that the visible-light response of **P25** – shown by the authors to be a mixture of anatase, rutile and amorphous phase [124] – is due to the presence of nano rutile domains amongst those of nano anatase. As such, they claimed that the points of contact between these anatase and rutile NPs allow for rapid electron transfer from rutile to anatase, hence making rutile an "antenna" able to extend the PCA into visible wavelengths.[125]

The PCA of the RE-TiO_2 under white light was much more dispersed away from the median value (horizontal dashed line in Fig. S8b†), with both more superior photocatalysts, and several poor photocatalysts. In general, 1 mol% RE addition achieved better results than 5 mol%, and the chloride salts with 1 mol% RE were the best performing photocatalysts, with the exception of **1%Nd_N_dp**. This gave the best result of all the

series, and of Nd-TiO_2, **1%Nd_N_dp** and **1%Nd_C_co** were both able to attain higher photodegradation performances than **P25**. Most likely, other samples suffered recombination of the e^-–h^+ photo-generated pairs, with doping-induced defects acting as recombination centers.[122] It is actually well established that PCA is affected by numerous parameters, *i.e.* phase composition, size of the photocatalyst, level of crystallinity, and surface properties (such as specific surface area, and/or surface hydroxyl groups).[126–129] **Furthermore, recent studies also highlighted the influence of microstructure on the photocatalytic property of TiO_2 based materials.**[130–132] **In these, it is stated that the combination of different TiO_2 polymorphs and microstructure can play a pivotal role in the PCA – more experimental work is currently being undertaken, so as to fully understand this behaviour.** In any case, the Achilles' heel of TiO_2 as a photocatalyst is reckoned to be the fast recombination rate of the photo-generated electron–hole pairs, though it is still greatly controversial where, when and how this phenomenon occurs.[133] Literature data report that the higher PCA under white light exposure of Nd-TiO_2 samples is attributable to the ability of neodymium doping to accelerate the interfacial electron transference process, and separate the photoexcited electrons and holes.[134] The introduction of Nd^{3+} 4*f* levels also play a crucial role in visible photosensitisation and enhancement of the electron–hole separation, enhancing the PCA under visible light irradiation.[135,136]

Moreover, the reaction path for NO_x conversion is mediated by $OH^\bullet$ radicals: during the photocatalytic reaction, O_2^- and $OH^\bullet$ radicals are formed and, as they react with the pollutant gas, HNO_3 is generated:[137]

$$(RE\text{-})TiO_2 + h\nu \rightarrow e_{CB}^- + h_{VB}^+ \quad (4)$$

$$h_{VB}^+ + H_2O_{(ads)} \rightarrow OH^\bullet + H^+ \quad (5)$$

$$h_{VB}^+ + OH^- \rightarrow OH^\bullet \quad (6)$$

$$e_{CB}^- + O_2 \rightarrow O_2^{\bullet-} \quad (7)$$

$$NO + OH^\bullet \rightarrow NO_2 + H^+ \quad (8)$$

$$NO + O_2^{\bullet-} \rightarrow NO_3^- \quad (9)$$

$$NO_2 + OH^\bullet \rightarrow NO_3^- + H^+ \rightarrow HNO_3 \quad (10)$$

Such HNO_3 is produced on the surface of the catalyst, and might act as a physical barrier, inhibiting the photocatalytic reaction.[138] Consequently, with the aim of verifying the stability and reproducibility with subsequent cycles of the best performing photocatalysts, tests were repeated in triplicate, using both lamps, the same samples and the same protocols as in the first run, but ending the repeated tests after 20 min of irradiation time.

Reproducibility results are depicted in Fig. 8a-d. It can be seen that using the solar lamp, Eu-TiO_2 photocatalysts are stable after the first run, with even **5%Eu_N_co**, the least stable, losing just 8% of its initial activity (Fig. 8a). On the contrary, Nd-TiO_2 seemed to be less stable compared to Eu-TiO_2: as shown in Fig. 8b, after the first run, all three selected samples lost 40-51% of their initial activity after one run, stabilising at around 35% NO_x abatement in the second and third runs. Under white-light (Fig. 8c,d) Eu-TiO_2 was shown to be very stable after two consecutive photocatalytic runs, and surprisingly, in case of **5%Eu_C_dp** and **1%Eu_C_co**, the PCA was even higher in the third consecutive run, reaching ~ 17% NO_x abatement. This indicates that a complete reuse cycle is possible for these photocatalysts. All three Nd-TiO_2 samples also showed themselves to be very stable after three consecutive photocatalytic runs, and suitable for reuse.

These results clearly showed that the photocatalysts did not suffer photocorrosion during the recycling tests, the HNO_3 formed did not have any significant negative effect on their PCA, and there was no leaching of REs from the photocatalysts, hence showing themselves to be very stable and reusable.

Conclusions

Nanopowders of titania and titania doped with Eu and Nd (1 and 5 mol%) were made by a green aqueous sol-gel route, using two different strategies for the RE doping. All of the RE-TiO_2 sols were stable systems, except for those based on europium and nitrate. The microstructure, optical properties, photocatalytic activity and photoluminescent properties of the synthetic nanomaterial were thoroughly evaluated.

RE addition heavily favoured brookite crystallisation, at the expense of rutile. It was also found that the Nd-TiO_2 sols, which had less variation in sol particle size than the Eu-TiO_2 sols, also had less variation in phase composition when fired at 450 ºC, and favoured anatase over rutile. The unit cell volume of RE-modified titania underwent a huge expansion, thus suggesting the incorporation of the RE into the TiO_2 lattice, accompanied by a decrease in the average crystalline domain diameters of anatase, rutile and brookite. All Re-TiO_2 samples were photocatalytically active under both solar and white-light exposure. Indeed, **1%Nd_N_co** under solar light, and **1%Nd_N_dp**, **1%Nd_C**_co and **1%Nd_C_dp** under white light, were superior to **P25**. They also did not suffer any significant photocorrosion during repeated cycle tests in the gas-solid phase, and there was no leaching of REs from the photocatalysts, showing them to be very stable and reusable. Moreover, both Eu-TiO_2 and Nd-TiO_2 exhibited photoluminescent behaviour. There were two distinct Nd^{3+} average local coordination sites, whilst all the Eu^{3+} ions occupied the same local environment. Furthermore, Nd-TiO_2 was shown to be a multifunctional material, having photocatalytic activity and NIR PL emission induced by the same excitation UV source, in first result of its kind.

These results suggest that RE-TiO_2 could potentially be used in environmental remediation, smart materials and display technologies.

Acknowledgements

D.M. Tobaldi is grateful to the ECO-SEE project (funding from the European Union's Seventh Framework Programme for

research, technological development and demonstration under grant agreement no 609234. *Note: The views expressed are purely those of the authors and may not in any circumstances be regarded as stating an official position of the European Commission*). R.C. Pullar acknowledges the support of FCT grant SFRH/BPD/97115/2013. This work was developed in the scope of the project CICECO−Aveiro Institute of Materials (Ref. FCT UID /CTM /50011/2013), financed by national funds through the FCT/MEC and when applicable co-financed by FEDER under the PT2020 Partnership Agreement. M. Ferro and RNME – University of Aveiro, FCT Project REDE/1509/RME/2005 – are also acknowledged for HR-TEM analysis.

Notes and references

[a] *Department of Materials and Ceramic Engineering / CICECO − Aveiro Institute of Materials, University of Aveiro, Campus Universitário de Santiago, 3810-193 Aveiro, Portugal.*
E-mail: david.tobaldi@ua.pt, david@davidtobaldi.org; Tel: +351 234 370 041.
[b] *Physics Department and CICECO − Aveiro Institute of Materials, University of Aveiro, Campus Universitário de Santiago, 3810-193 Aveiro, Portugal.*

† Electronic Supplementary Information (ESI) available: [experimental procedure of PCA in the liquid-solid phase; PCA in liquid-solid phase; emission spectra of the lamp used for the PCA tests; Rietveld and WPPM graphical outputs; size distribution obtained from WPPM modelling of selected samples; Plot of diffuse reflectance first derivative *versus* wavelength λ of sample **5%Eu_N_dp**; scattered plots of PCA results in gas-solid phase]. See DOI: 10.1039/b000000x/

1 I. B. Gosbell, *Am. J. Clin. Dermatol.*, 2004, **5**, 239–259.
2 H. Tong, S. Ouyang, Y. Bi, N. Umezawa, M. Oshikiri and J. Ye, *Adv. Mater.*, 2012, **24**, 229–251.
3 I. K. Konstantinou and T. A. Albanis, *Appl. Catal. B Environ.*, 2004, **49**, 1–14.
4 J. L. Repace, *Environ. Int.*, 1982, **8**, 21–36.
5 A. P. Jones, *Atmos. Environ.*, 1999, **33**, 4535–4564.
6 A. Fujishima, X. Zhang and D. Tryk, *Surf. Sci. Rep.*, 2008, **63**, 515–582.
7 L. Kavan, *Chem. Rec.*, 2012, **12**, 131–142.
8 M. Grätzel, *J. Photochem. Photobiol. C Photochem. Rev.*, 2003, **4**, 145–153.
9 K. Sunada, Y. Kikuchi, K. Hashimoto and A. Fujishima, *Environ. Sci. Technol.*, 1998, **32**, 726–728.
10 K. Sunada, T. Watanabe and K. Hashimoto, *J. Photochem. Photobiol. Chem.*, 2003, **156**, 227–233.
11 S. A. Grinshpun, A. Adhikari, T. Honda, K. Y. Kim, M. Toivola, K. S. Ramchander Rao and T. Reponen, *Environ. Sci. Technol.*, 2007, **41**, 606–612.
12 K. Kowal, K. Wysocka-Król, M. Kopaczyńska, E. Dworniczek, R. Franiczek, M. Wawrzyńska, M. Vargová, M. Zahoran, E. Rakovský, P. Kuš, G. Plesch, A. Plecenik, F. Laffir, S. A. M. Tofail and H. Podbielska, *J. Colloid Interface Sci.*, 2011, **362**, 50–57.
13 J.-M. Herrmann, C. Duchamp, M. Karkmaz, B. T. Hoai, H. Lachheb, E. Puzenat and C. Guillard, *J. Hazard. Mater.*, 2007, **146**, 624–629.
14 S.-D. Mo and W. Y. Ching, *Phys. Rev. B*, 1995, **51**, 13023–13032.
15 Z. Şen, *Solar energy fundamentals and modeling techniques: atmosphere, environment, climate change, and renewable energy*, Springer, London, 2008.
16 R. Asahi, T. Morikawa, T. Ohwaki, K. Aoki and Y. Taga, *Science*, 2001, **293**, 269–271.
17 D. M. Tobaldi, L. Gao, A. F. Gualtieri, A. Sever Škapin, A. Tucci and C. Giacobbe, *J. Am. Ceram. Soc.*, 2012, **95**, 1709–1716.
18 M. Anpo, *Pure Appl. Chem.*, 2000, **72**, 1787–1792.
19 P. Wang, B. Huang, Y. Dai and M.-H. Whangbo, *Phys. Chem. Chem. Phys.*, 2012, **14**, 9813.
20 D. M. Tobaldi, R. C. Pullar, A. F. Gualtieri, M. P. Seabra and J. A. Labrincha, *Chem. Eng. J.*, 2013, **214**, 364–375.
21 D. M. Tobaldi, C. Piccirillo, R. C. Pullar, A. F. Gualtieri, M. P. Seabra, P. M. L. Castro and J. A. Labrincha, *J. Phys. Chem. C*, 2014, **118**, 4751–4766.
22 Y. Li, H. Zhang, Z. Guo, J. Han, X. Zhao, Q. Zhao and S.-J. Kim, *Langmuir*, 2008, **24**, 8351–8357.
23 W. Sun, Y. Li, W. Shi, X. Zhao and P. Fang, *J. Mater. Chem.*, 2011, **21**, 9263.
24 J. Tian, Y. Sang, G. Yu, H. Jiang, X. Mu and H. Liu, *Adv. Mater.*, 2013, **25**, 5075–5080.
25 Y. Ma, Y. Li, M. Mao, J. Hou, M. Zeng and X. Zhao, *J Mater Chem A*, 2015, **3**, 5509–5516.
26 J. Hou, Y. Li, M. Mao, Y. Yue, G. N. Greaves and X. Zhao, *Nanoscale*, 2015, **7**, 2633–2640.
27 X. Wu, S. Yin, Q. Dong, B. Liu, Y. Wang, T. Sekino, S. W. Lee and T. Sato, *Sci. Rep.*, 2013, **3**.
28 S. Bingham and W. A. Daoud, *J. Mater. Chem.*, 2011, **21**, 2041–2050.
29 A. S. Weber, A. M. Grady and R. T. Koodali, *Catal. Sci. Technol.*, 2012, **2**, 683–693.
30 D. M. Tobaldi, A. Sever Škapin, R. C. Pullar, M. P. Seabra and J. A. Labrincha, *Ceram. Int.*, 2013, **39**, 2619–2629.
31 D. M. Tobaldi, R. C. Pullar, A. S. Škapin, M. P. Seabra and J. A. Labrincha, *Mater. Res. Bull.*, 2014, **50**, 183–190.
32 J. Reszczyńska, T. Grzyb, J. W. Sobczak, W. Lisowski, M. Gazda, B. Ohtani and A. Zaleska, *Appl. Surf. Sci.*
33 J. Reszczyńska, T. Grzyb, J. W. Sobczak, W. Lisowski, M. Gazda, B. Ohtani and A. Zaleska, *Appl. Catal. B Environ.*, 2015, **163**, 40–49.
34 J. Lin and J. C. Yu, *J. Photochem. Photobiol. Chem.*, 1998, **116**, 63–67.
35 V. Štengl, S. Bakardjieva and N. Murafa, *Mater. Chem. Phys.*, 2009, **114**, 217–226.
36 G. Feng, S. Liu, Z. Xiu, Y. Zhang, J. Yu, Y. Chen, P. Wang and X. Yu, *J. Phys. Chem. C*, 2008, **112**, 13692–13699.
37 A. A. Bol, R. van Beek and A. Meijerink, *Chem. Mater.*, 2002, **14**, 1121–1126.
38 W. Chen, J. Z. Zhang and A. G. Joly, *J. Nanosci. Nanotechnol.*, 2004, **4**, 919–947.
39 M. Klik, T. Gregorkiewicz, I. Bradley and J.-P. Wells, *Phys. Rev. Lett.*, 2002, **89**.
40 N. M. Idris, S. S. Lucky, Z. Li, K. Huang and Y. Zhang, *J Mater Chem B*, 2014, **2**, 7017–7026.
41 C.-H. Liang, M.-F. Hou, S.-G. Zhou, F.-B. Li, C.-S. Liu, T.-X. Liu, Y.-X. Gao, X.-G. Wang and J.-L. Lü, *J. Hazard. Mater.*, 2006, **138**, 471–478.
42 F. B. Li, X. Z. Li, C. H. Ao, S. C. Lee and M. F. Hou, *Chemosphere*, 2005, **59**, 787–800.
43 K. M. Parida and N. Sahu, *J. Mol. Catal. Chem.*, 2008, **287**, 151–158.
44 K. T. Ranjit, I. Willner, S. H. Bossmann and A. M. Braun, *Environ. Sci. Technol.*, 2001, **35**, 1544–1549.
45 A.-W. Xu, Y. Gao and H.-Q. Liu, *J. Catal.*, 2002, **207**, 151–157.
46 Y. Yang, C. Zhang, Y. Xu, H. Wang, X. Li and C. Wang, *Mater. Lett.*, 2010, **64**, 147–150.
47 I. Cacciotti, A. Bianco, G. Pezzotti and G. Gusmano, *Chem. Eng. J.*, 2011, **166**, 751–764.
48 J. Castañeda-Contreras, M. A. Meneses-Nava, O. Barbosa-García, J. L. Maldonado-Rivera and J. F. Mosiño, *Opt. Mater.*, 2004, **27**, 301–305.
49 J. Castañeda, *J. Rare Earths*, 2011, **29**, 420–425.
50 L. Li, C.-K. Tsung, Z. Yang, G. D. Stucky, L. D. Sun, J. F. Wang and C. H. Yan, *Adv. Mater.*, 2008, **20**, 903–908.
51 X. Mao, B. Yan, J. Wang and J. Shen, *Vacuum*, 2014, **102**, 38–42.
52 A. Patra, C. S. Friend, R. Kapoor and P. N. Prasad, *Chem. Mater.*, 2003, **15**, 3650–3655.
53 S. M. Mukhopadhyay, Ed., *Nanoscale Multifunctional Materials: Science and Applications*, John Wiley & Sons, Inc., Hoboken, NJ, USA, 2011.
54 D. Maspoch, D. Ruiz-Molina and J. Veciana, *Chem. Soc. Rev.*, 2007, **36**, 770.
55 E. Chelebaeva, J. Larionova, Y. Guari, R. A. S. Ferreira, L. D. Carlos, F. A. A. Paz, A. Trifonov and C. Guérin, *Inorg. Chem.*, 2009, **48**, 5983–5995.

56 S. Chorazy, K. Nakabayashi, M. Arczynski, R. Pełka, S. Ohkoshi and B. Sieklucka, *Chem. - Eur. J.*, 2014, **20**, 7144–7159.
57 J. Long, R. Vallat, R. A. S. Ferreira, L. D. Carlos, F. A. Almeida Paz, Y. Guari and J. Larionova, *Chem. Commun.*, 2012, **48**, 9974.
58 D. M. Tobaldi, R. C. Pullar, R. Binions, A. Belen Jorge, P. F. McMillan, M. Saeli, M. P. Seabra and J. A. Labrincha, *Catal. Sci. Technol.*, 2014, **4**, 2134.
59 W. Luo, R. Li, G. Liu, M. R. Antonio and X. Chen, *J. Phys. Chem. C*, 2008, **112**, 10370–10377.
60 D. M. Tobaldi, R. C. Pullar, A. F. Gualtieri, M. P. Seabra and J. A. Labrincha, *Acta Mater.*, 2013, **61**, 5571–5585.
61 A. C. Larson and R. B. Von Dreele, *General Structure Analysis System (GSAS)*, Los Alamos National Laboratory Report LAUR, 2004.
62 B. H. Toby, *J. Appl. Crystallogr.*, 2001, **34**, 210–213.
63 P. Scardi and M. Leoni, *Acta Crystallogr. A*, 2002, **58**, 190–200.
64 M. Leoni, T. Confente and P. Scardi, *Z. Für Krist. Suppl.*, 2006, **23**, 249–254.
65 P. Scardi and M. Leoni, in *Diffraction Analysis of the Microstructure of Materials*, Eric J. Mittemeijer, Paolo Scardi, Berlin, Springer-Verlag., 2004, pp. 51–92.
66 P. Scardi and M. Leoni, *J. Appl. Crystallogr.*, 2006, **39**, 24–31.
67 H. P. Klug and L. E. Alexander, *X-ray diffraction procedures for polycrystalline and amorphous materials*, Wiley, New York, 2nd Edition., 1974.
68 G. K. Williamson and W. H. Hall, *Acta Metall.*, 1953, **1**, 22–31.
69 P. Scardi and M. Leoni, *Acta Mater.*, 2005, **53**, 5229–5239.
70 G. Caglioti, A. Paoletti and F. P. Ricci, *Nucl. Instrum. Methods*, 1960, **9**, 195–198.
71 A. S. Marfunin, *Physics of minerals and inorganic materials : an introduction*, Springer-Verlag, Berlin; New York, 1979.
72 S. Komornicki, M. Radecka and P. Sobaś, *Mater. Res. Bull.*, 2004, **39**, 2007–2017.
73 M. Vautier, C. Guillard and J.-M. Herrmann, *J. Catal.*, 2001, **201**, 46–59.
74 X. Yan, T. Ohno, K. Nishijima, R. Abe and B. Ohtani, *Chem. Phys. Lett.*, 2006, **429**, 606–610.
75 J.-M. Herrmann, *Appl. Catal. B Environ.*, 2010, **99**, 461–468.
76 J.-M. Herrmann, *J. Photochem. Photobiol. Chem.*, 2010, **216**, 85–93.
77 S. S. Lucas, V. M. Ferreira and J. L. B. de Aguiar, *Cem. Concr. Res.*, 2013, **43**, 112–120.
78 *Philips.com*, 2014.
79 A. J. Lawrence, A. Masih and A. Taneja, *Indoor Air*, 2005, **15**, 76–82.
80 *WHO - Guidel. Indoor Air Qual. Sel. Pollut.*, 2010.
81 U. I. Gaya and A. H. Abdullah, *J. Photochem. Photobiol. C Photochem. Rev.*, 2008, **9**, 1–12.
82 F. L. Toma, G. Bertrand, D. Klein and C. Coddet, *Environ. Chem. Lett.*, 2004, **2**, 117–121.
83 D. Nassoko, Y.-F. Li, J.-L. Li, X. Li and Y. Yu, *Int. J. Photoenergy*, 2012, **2012**, 1–10.
84 J. Ovenstone, P. J. Titler, R. Withnall and J. Silver, *J. Phys. Chem. B*, 2001, **105**, 7170–7177.
85 N. Paul and D. Mohanta, *J. Mater. Res.*, 2013, **28**, 1471–1480.
86 S. L. Isley and R. L. Penn, *J. Phys. Chem. B*, 2006, **110**, 15134–15139.
87 H. Zhang, M. Finnegan and J. F. Banfield, *Nano Lett.*, 2001, **1**, 81–85.
88 Y. Hu, H.-L. Tsai and C.-L. Huang, *Mater. Sci. Eng. A*, 2003, **344**, 209–214.
89 D. M. Tobaldi, R. C. Pullar, A. F. Gualtieri, A. Belen Jorge, R. Binions, P. F. McMillan, M. P. Seabra and J. A. Labrincha, *CrystEngComm*, 2015, **17**, 1813–1825.
90 A. Pottier, C. Chanéac, E. Tronc, L. Mazerolles and J.-P. Jolivet, *J. Mater. Chem.*, 2001, **11**, 1116–1121.
91 Y. Hu, H.-L. Tsai and C.-L. Huang, *J. Eur. Ceram. Soc.*, 2003, **23**, 691–696.
92 D. Reyes-Coronado, G. Rodríguez-Gattorno, M. E. Espinosa-Pesqueira, C. Cab, R. de Coss and G. Oskam, *Nanotechnology*, 2008, **19**, 145605.
93 J.-G. Li and T. Ishigaki, *Acta Mater.*, 2004, **52**, 5143–5150.
94 R. D. Shannon, *Acta Crystallogr. Sect. A*, 1976, **32**, 751–767.
95 P. Ghigna, A. Speghini and M. Bettinelli, *J. Solid State Chem.*, 2007, **180**, 3296–3301.
96 P. Ghosh, K. R. Priolkar and A. Patra, *J. Phys. Chem. C*, 2007, **111**, 571–578.
97 M. Pal, U. Pal, J. M. G. Y. Jiménez and F. Pérez-Rodríguez, *Nanoscale Res. Lett.*, 2012, **7**, 1.
98 Ž. Antić, R. M. Krsmanović, M. G. Nikolić, M. Marinović-Cincović, M. Mitrić, S. Polizzi and M. D. Dramićanin, *Mater. Chem. Phys.*, 2012, **135**, 1064–1069.
99 E. Le Boulbar, E. Millon, E. Ntsoenzok, B. Hakim, W. Seiler, C. Boulmer-Leborgne and J. Perrière, *Opt. Mater.*, 2012, **34**, 1419–1425.
100 K. Bouras, J.-L. Rehspringer, G. Schmerber, H. Rinnert, S. Colis, G. Ferblantier, M. Balestrieri, D. Ihiawakrim, A. Dinia and A. Slaoui, *J Mater Chem C*, 2014, **2**, 8235–8243.
101 E. Stoyanov, F. Langenhorst and G. Steinle-Neumann, *Am. Mineral.*, 2007, **92**, 577–586.
102 Q. G. Zeng, Z. J. Ding and Z. M. Zhang, *J. Lumin.*, 2006, **118**, 301–307.
103 F. C. Hawthorne and Mineralogical Society of America, Eds., *Spectroscopic methods in mineralogy and geology*, Mineralogical Society of America, Washington, D.C., 1988.
104 A. de Bettencourt-Dias, Ed., *Luminescence of lanthanide ions in coordination compounds and nanomaterials*, John Wiley & Sons Inc, Chichester, West Sussex, United Kingdom, 2014.
105 B.-H. Jung, D.-K. Lee, S.-H. Sohn and H.-S. Kim, *J. Am. Ceram. Soc.*, 2003, **86**, 1202–1204.
106 W. T. Carnall, *J. Chem. Phys.*, 1968, **49**, 4412.
107 B. Judd, *Phys. Rev.*, 1962, **127**, 750–761.
108 N. Wang, W. Jiang, X. Xu, Z. Si, H. Bai and C. Tian, *Anal. Sci.*, 2002, **18**, 591–594.
109 B. Ohtani, *J. Photochem. Photobiol. C Photochem. Rev.*, 2010, **11**, 157–178.
110 H. Tang, H. Berger, P. E. Schmid, F. Lévy and G. Burri, *Solid State Commun.*, 1993, **87**, 847–850.
111 M. Koelsch, S. Cassaignon, J. . Guillemoles and J. . Jolivet, *Thin Solid Films*, 2002, **403-404**, 312–319.
112 M. Landmann, E. Rauls and W. G. Schmidt, *J. Phys. Condens. Matter*, 2012, **24**, 195503.
113 A. Di Paola, M. Bellardita and L. Palmisano, *Catalysts*, 2013, **3**, 36–73.
114 S. Kumar, Z. Jindal, N. Kumari and N. K. Verma, *J. Nanoparticle Res.*, 2011, **13**, 5465–5471.
115 E. Le Boulbar, E. Millon, C. Boulmer-Leborgne, C. Cachoncinlle, B. Hakim and E. Ntsoenzok, *Thin Solid Films*, 2014, **553**, 13–16.
116 K. L. Frindell, M. H. Bartl, A. Popitsch and G. D. Stucky, *Angew. Chem. Int. Ed.*, 2002, **41**, 959–962.
117 K. L. Frindell, M. H. Bartl, M. R. Robinson, G. C. Bazan, A. Popitsch and G. D. Stucky, *J. Solid State Chem.*, 2003, **172**, 81–88.
118 D. F. Ollis and H. Al-Ekabi, *Photocatalytic purification and treatment of water and air*, Elsevier, 1993.
119 J. Zhang, *Self-Assembled Nanostructures*, Springer Science & Business Media, 2003.
120 M. Addamo, V. Augugliaro, S. Coluccia, A. D. Paola, E. García-López, V. Loddo, G. Marcì, G. Martra and L. Palmisano, *Int. J. Photoenergy*, 2006, **2006**, 1–12.
121 M. Bettinelli, A. Speghini, D. Falcomer, M. Daldosso, V. Dallacasa and L. Romanò, *J. Phys. Condens. Matter*, 2006, **18**, S2149–S2160.
122 M. Kong, Y. Li, X. Chen, T. Tian, P. Fang, F. Zheng and X. Zhao, *J. Am. Chem. Soc.*, 2011, **133**, 16414–16417.
123 S. Yin, H. Hasegawa, D. Maeda, M. Ishitsuka and T. Sato, *J. Photochem. Photobiol. Chem.*, 2004, **163**, 1–8.
124 D. M. Tobaldi, R. C. Pullar, M. P. Seabra and J. A. Labrincha, *Mater. Lett.*, 2014, **122**, 345–347.
125 D. C. Hurum, A. G. Agrios, K. A. Gray, T. Rajh and M. C. Thurnauer, *J. Phys. Chem. B*, 2003, **107**, 4545–4549.
126 G. Balasubramanian, D. D. Dionysiou, M. T. Suidan, I. Baudin and J.-M. Laîné, *Appl. Catal. B Environ.*, 2004, **47**, 73–84.
127 M. R. Hoffmann, S. T. Martin, W. Choi and D. W. Bahnemann, *Chem. Rev.*, 1995, **95**, 69–96.
128 N. Serpone and E. Pelizzetti, *Photocatalysis: fundamentals and applications*, Wiley, New York, 1989.
129 Z. Zhang, C.-C. Wang, R. Zakaria and J. Y. Ying, *J. Phys. Chem. B*, 1998, **102**, 10871–10878.
130 R. L. Penn and J. F. Banfield, *Geochim. Cosmochim. Acta*, 1999, 63, 1549–1557.
131 A. Chowdhury, A. Kudo, T. Fujita, M.-W. Chen and T. Adschiri, *J. Supercrit. Fluids*, 2011, 58, 136–141.

132 F. Dufour, S. Pigeot-Remy, O. Durupthy, S. Cassaignon, V. Ruaux, S. Torelli, L. Mariey, F. Maugé and C. Chanéac, *Appl. Catal. B Environ.*, 2015, 174–175, 350–360.
133 B. Ohtani, *Catalysts*, 2013, **3**, 942–953.
134 Y. Xie and C. Yuan, *Appl. Surf. Sci.*, 2004, **221**, 17–24.
135 F. B. Li, X. Z. Li and K. W. Cheah, *Environ. Chem.*, 2005, **2**, 130.
136 S. Rengaraj, S. Venkataraj, J.-W. Yeon, Y. Kim, X. Z. Li and G. K. H. Pang, *Appl. Catal. B Environ.*, 2007, **77**, 157–165.
137 J. Lasek, Y.-H. Yu and J. C. S. Wu, *J. Photochem. Photobiol. C Photochem. Rev.*, 2013, **14**, 29–52.
138 Y. Ohko, Y. Nakamura, A. Fukuda, S. Matsuzawa and K. Takeuchi, *J. Phys. Chem. C*, 2008, **112**, 10502–10508.

Figure and Captions

Fig. 1 – Schematic diagram of the synthesis process to form the 16 RE-doped titania nanopowder samples.

Fig. 2 – Raman spectra of selected samples – the vertical bars represent the Raman peak shifts of: anatase (red), rutile (black), and brookite (blue).[58] In the inset is shown a magnification between 100-200 cm^{-1}, to highlight the peak broadening and red shifting of the Raman E_g active mode of anatase at 144 cm^{-1} (the vertical dashed line indicates the position of that peak in the undoped TiO_2 sample).

Fig. 3 – HR-TEM micrographs of: a) undoped **TiO_2**; b) **1%Eu_C_co**; c) **1%Nd_N_dp**. The *d*-spacing of (101) anatase (Ant), and (110) rutile (Rut) crystallographic planes is shown in the Figures.

Fig. 4 – Diffuse reflectance spectra of: a) sample **5%Eu_N_co**; peaks at 465 and 532 nm are marked; b) sample **5%Nd_N_co**; peaks at 528, 586 and 684 nm are marked (for their interpretation, please refer to the text).

Fig.5 – a) Emission and b) excitation spectra of **1%Nd_N_dp**, **1%Nd_C_co** and **1%Nd_N_co**, excited at 390 nm (black) and 584 nm (blue) and monitored at 1070 nm (black) and 1090 nm (blue), respectively.

Fig. 6 – a) Emission and b) excitation spectra of **1%Eu_C_dp** and **1%Eu_C_co**, excited at 465 nm and monitored at 612 nm, respectively.

Fig. 7 – Photocatalytic activity results in the gas-solid phase, considered as the initial (20 min) pseudo-first order kinetic constants, k'_{app}, using a) the solar lamp; b) the white LED lamp.

Fig. 8 – Photocatalytic tests recycling, in the gas-solid phase, of selected Eu- and Nd-TiO_2 samples. a) Eu-TiO_2 using the solar lamp; b) Nd-TiO_2 using the solar lamp; c) Eu-TiO_2 using the white LED lamp; d) Nd-TiO_2 using the white LED lamp.

Fig. 1

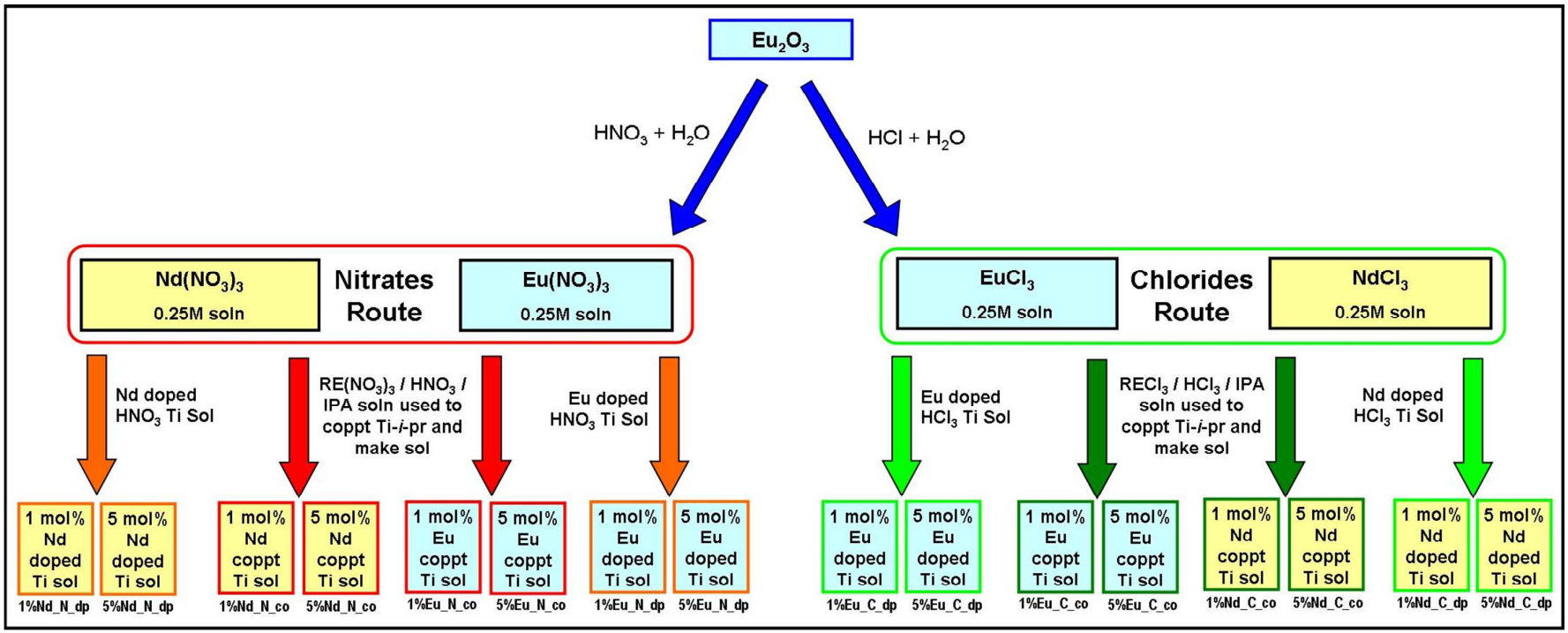

Fig. 2

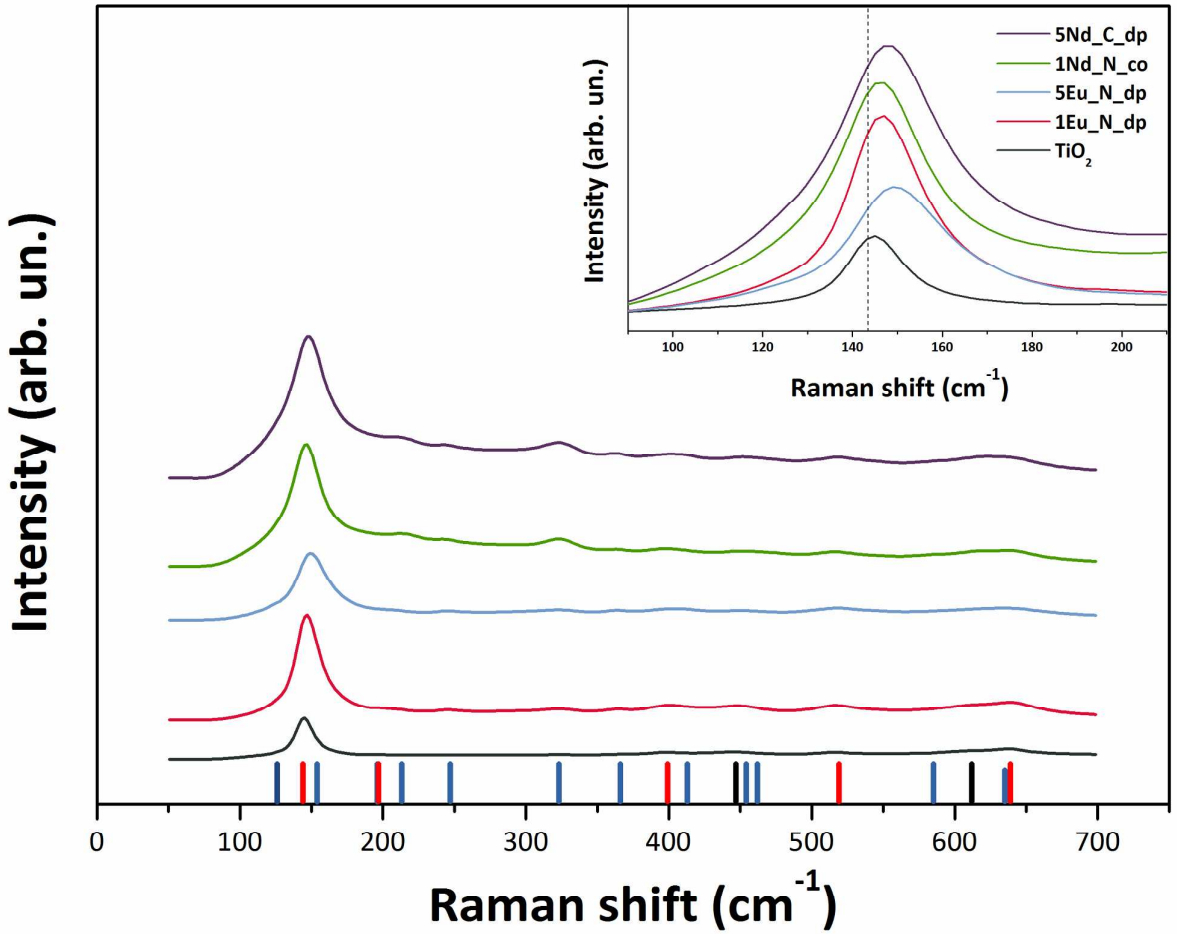

Fig. 3a

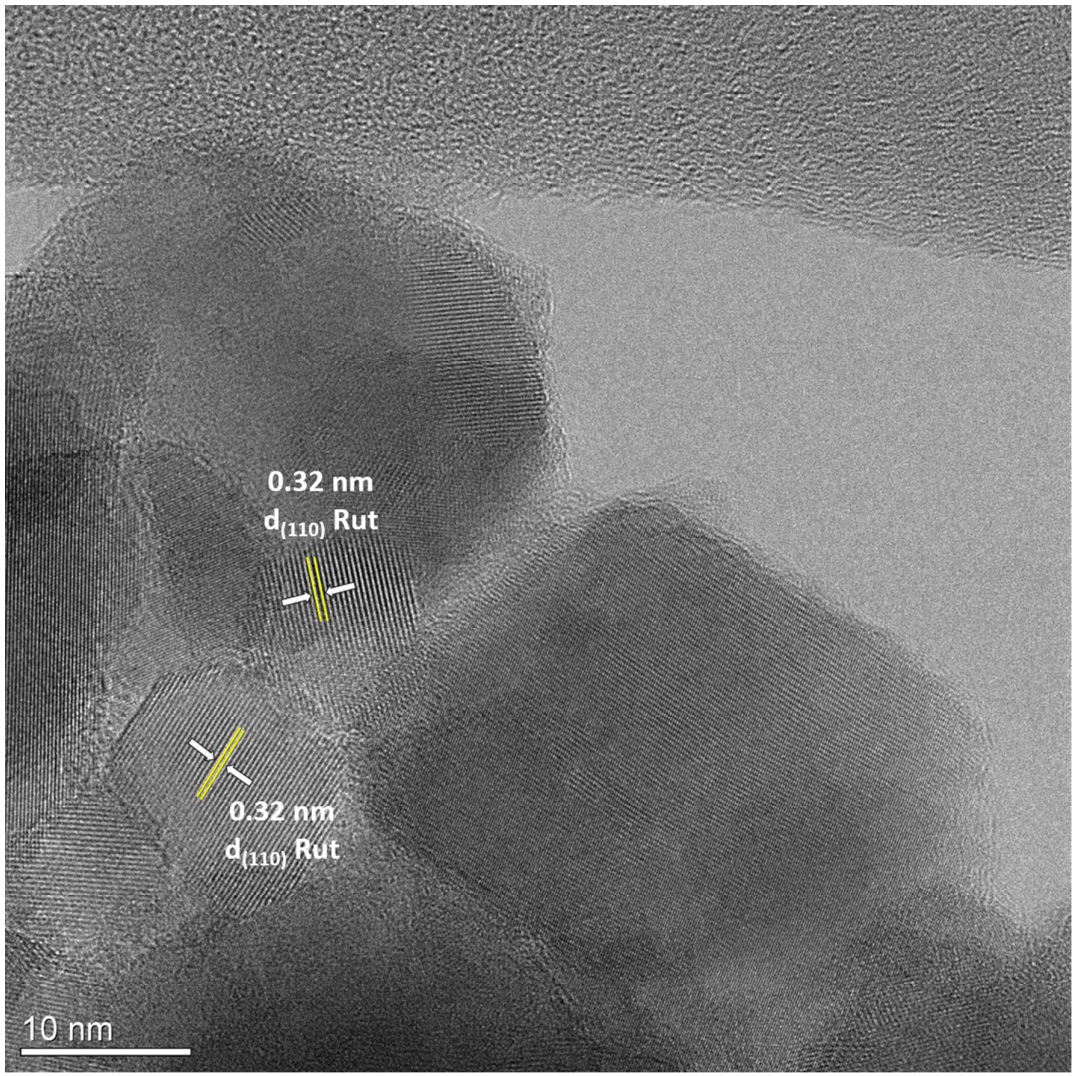

Fig. 3b

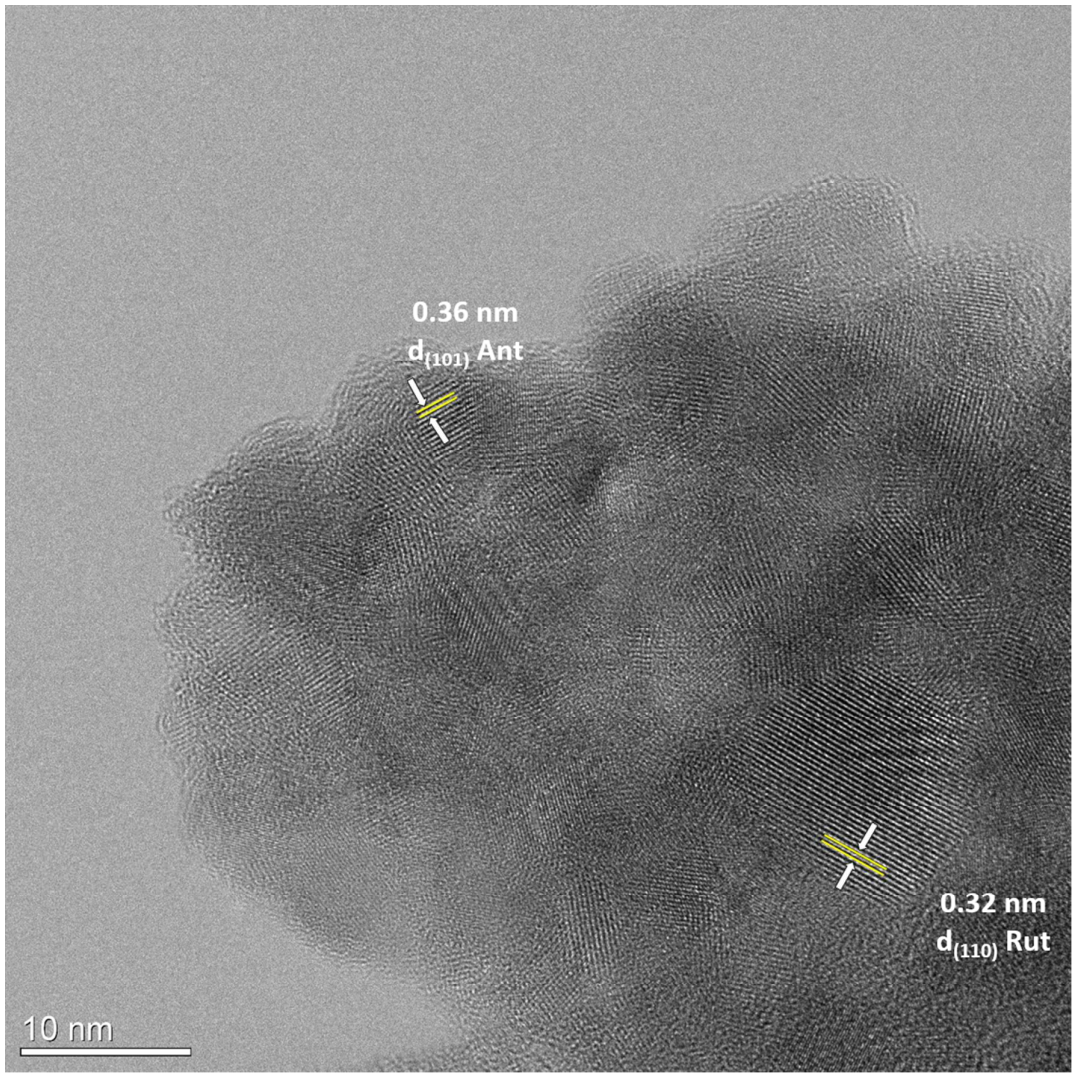

Fig.3c

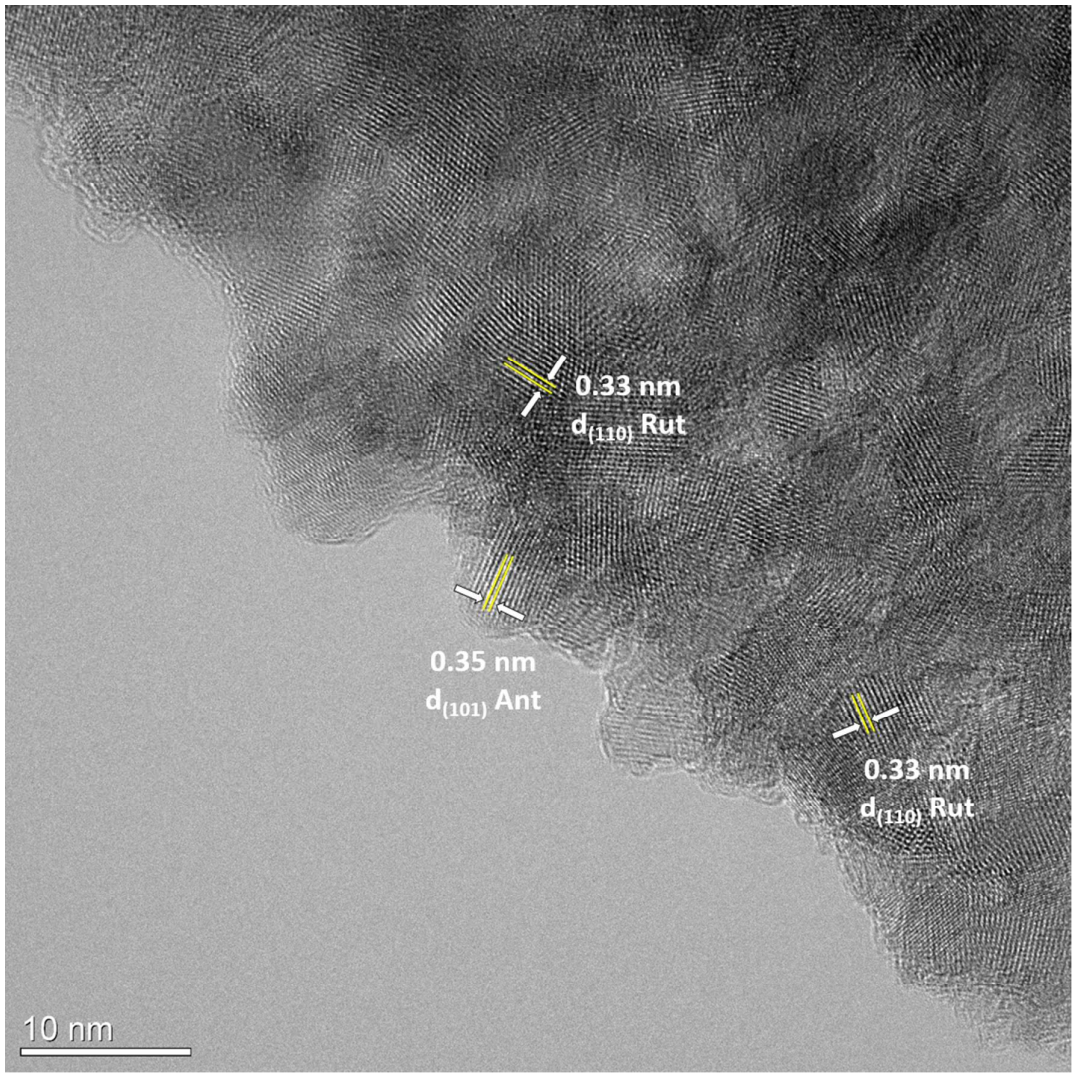

Fig. 4

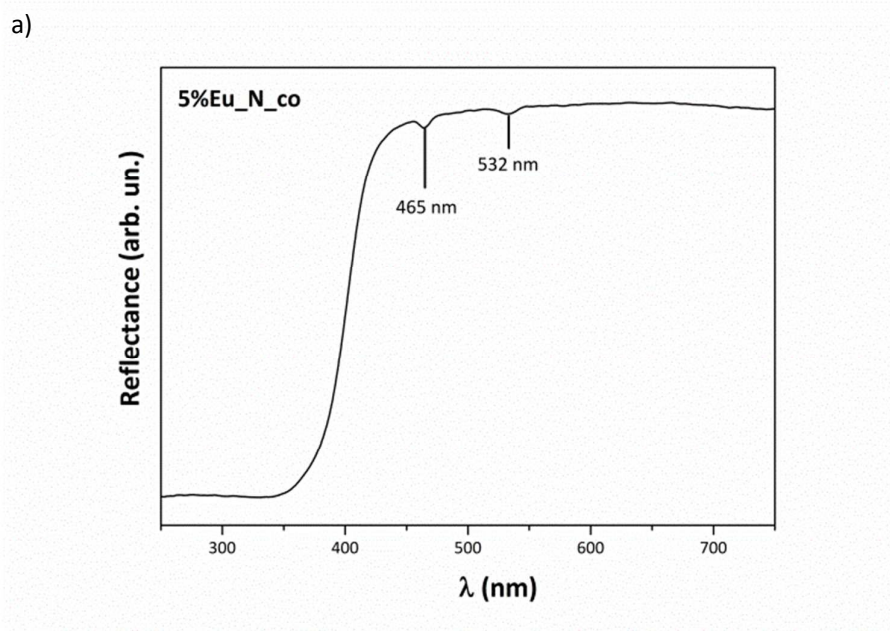

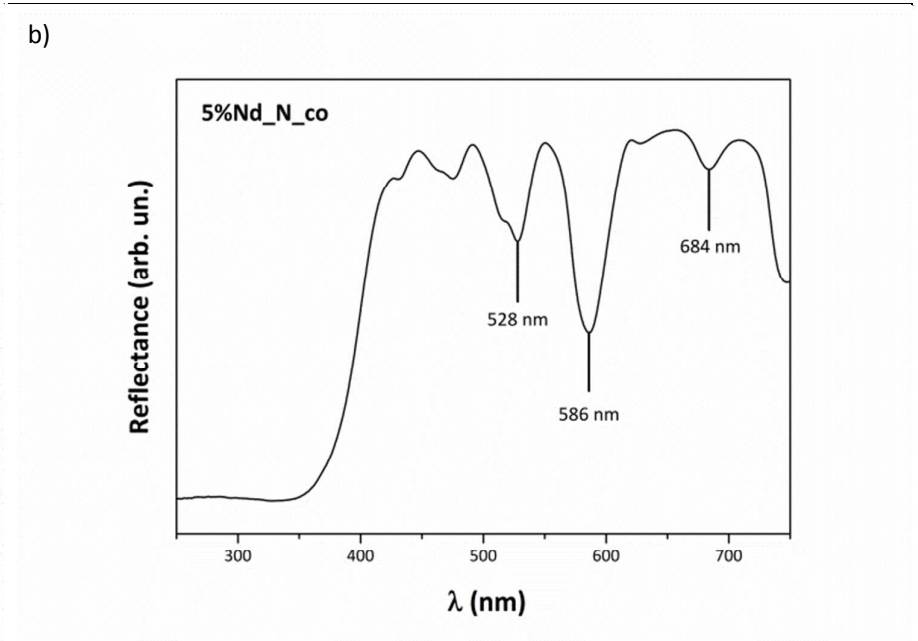

Fig. 5a

a)

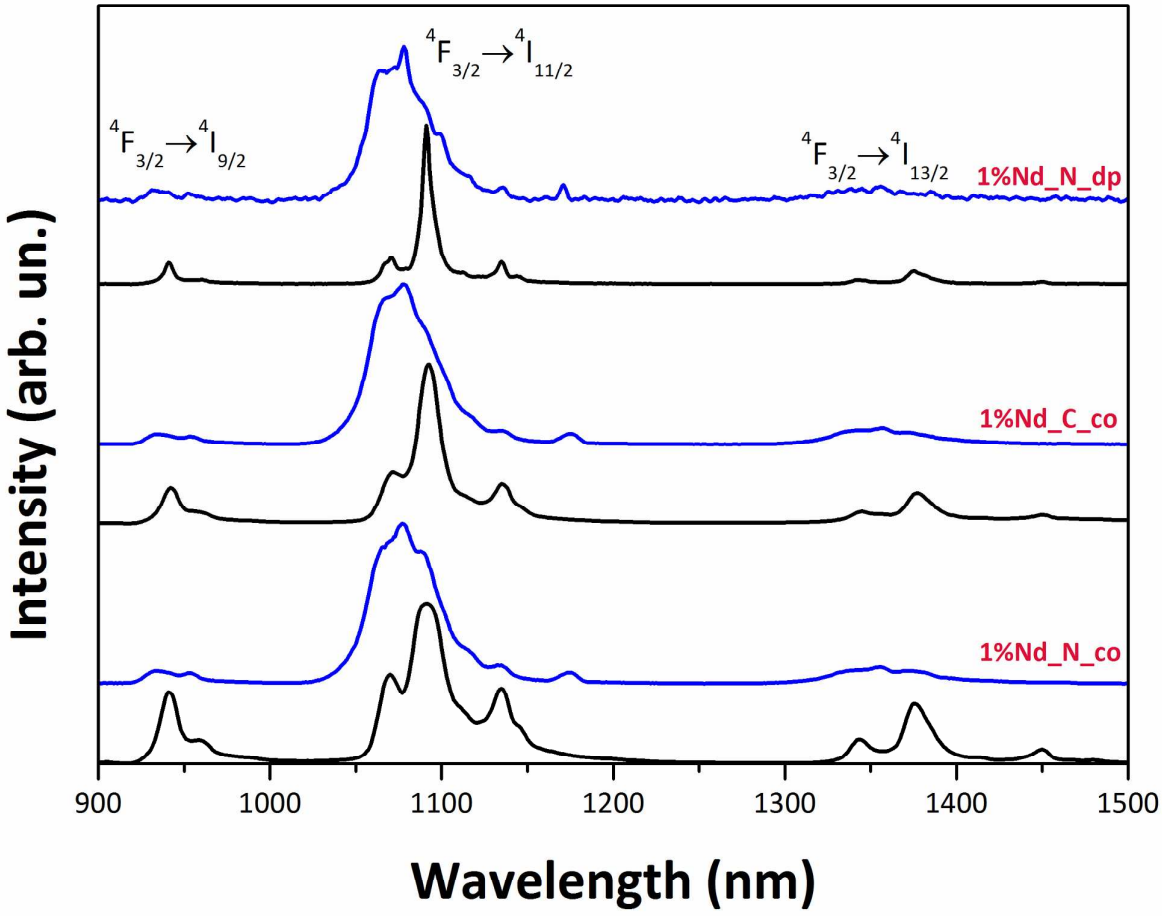

Fig. 5b

b)

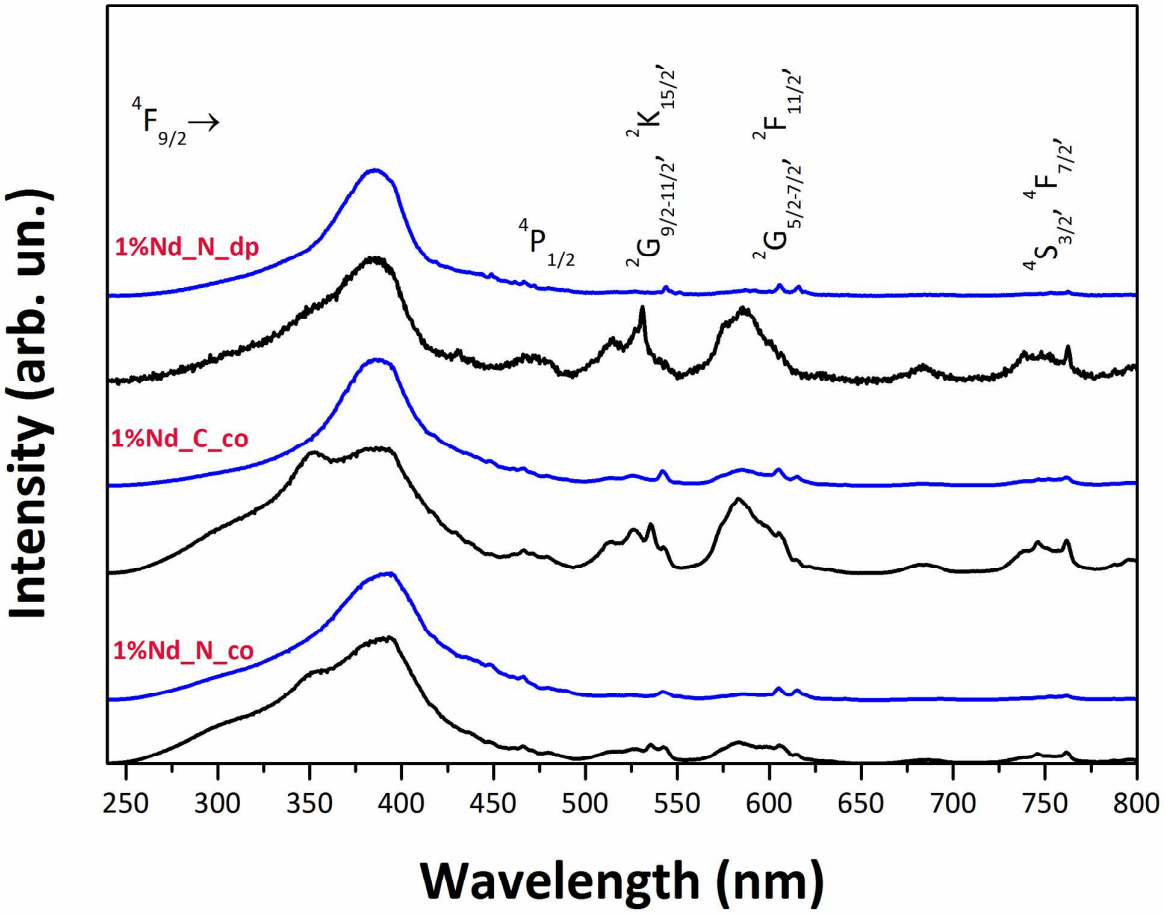

Fig. 6a

a)

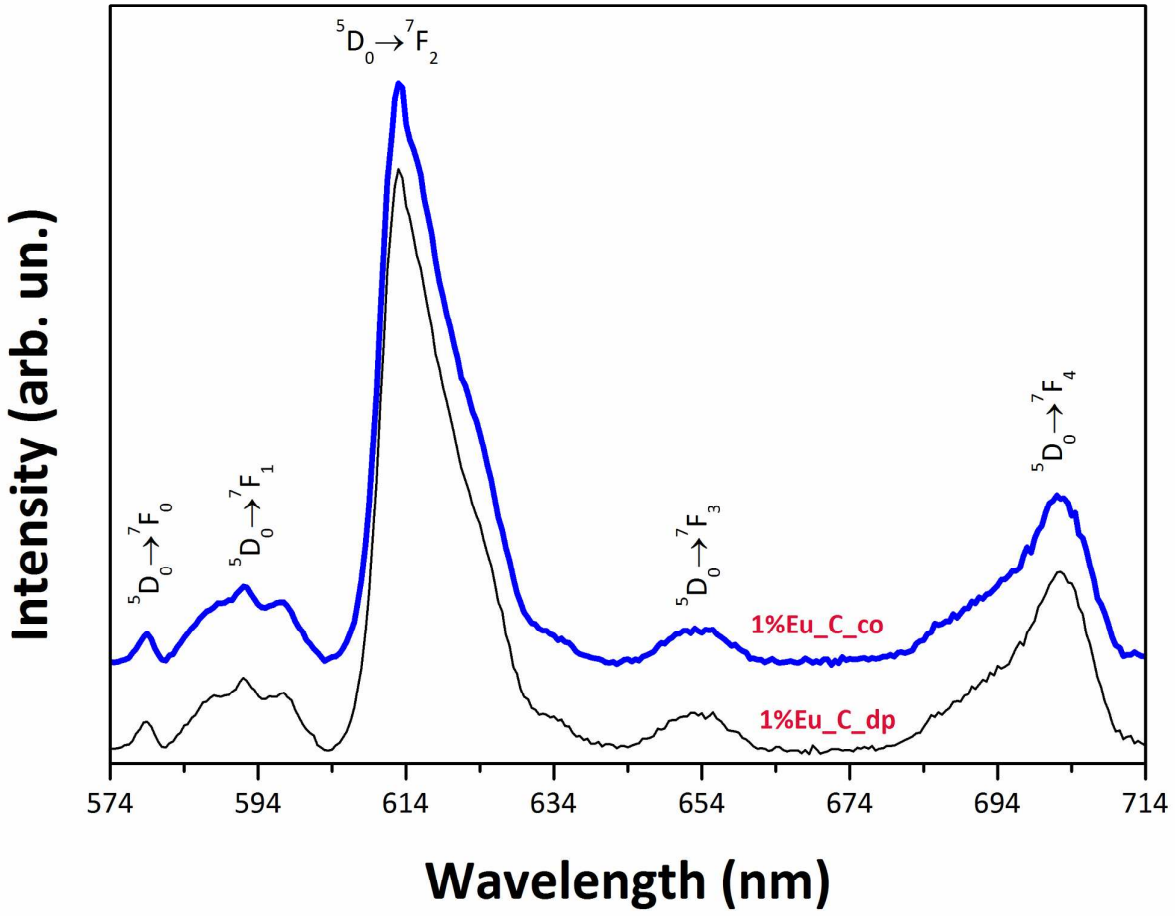

Fig. 6b

b)

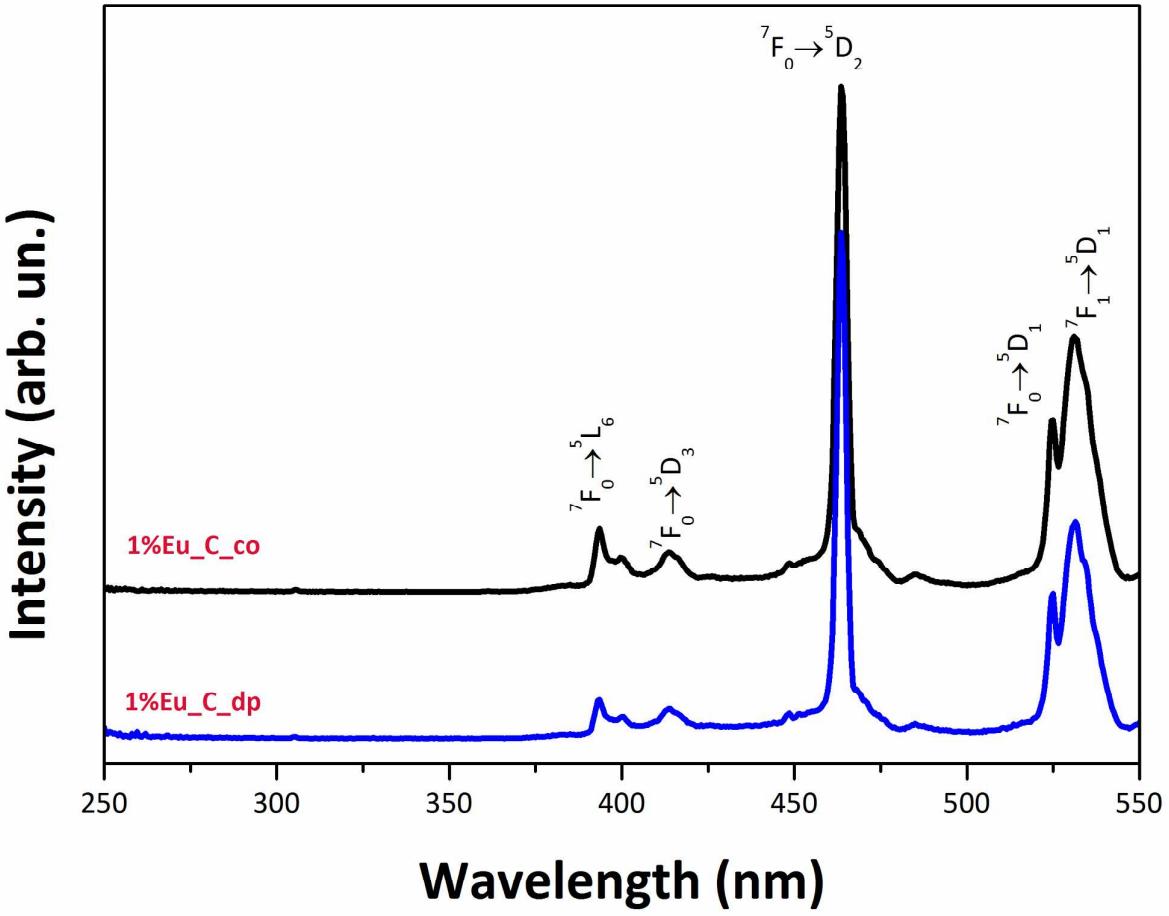

Fig. 7a

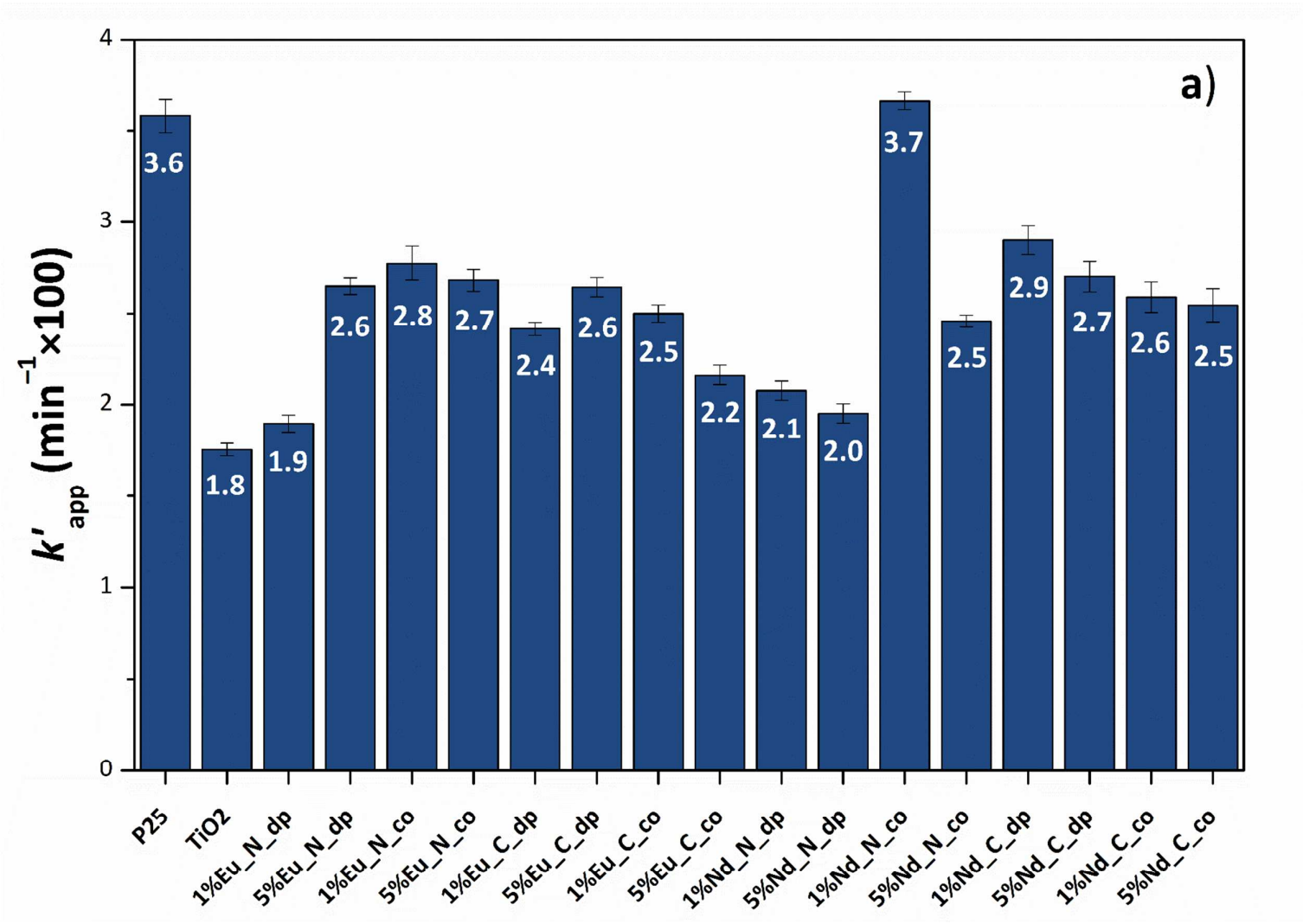

Fig. 7b

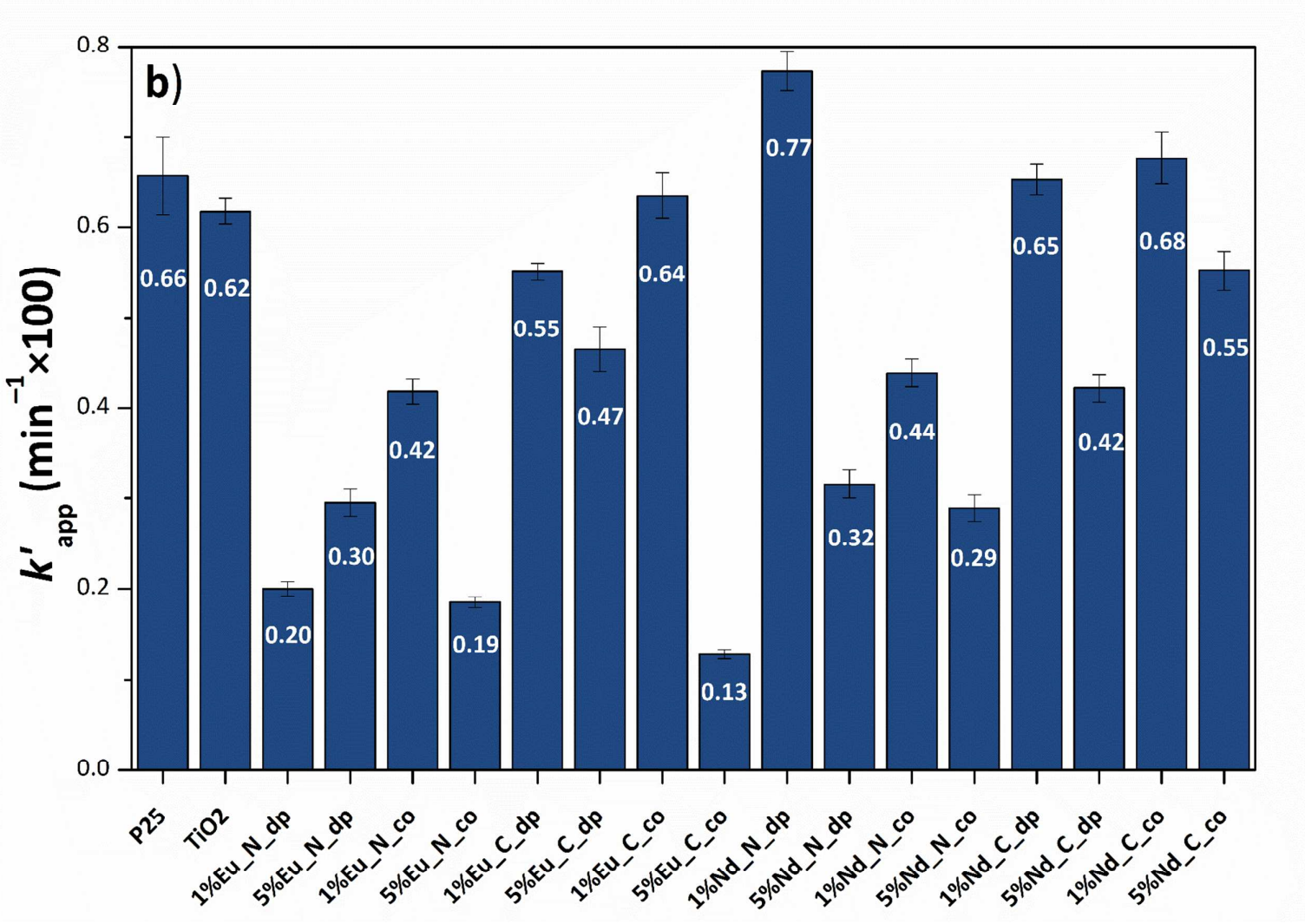

Fig. 8a

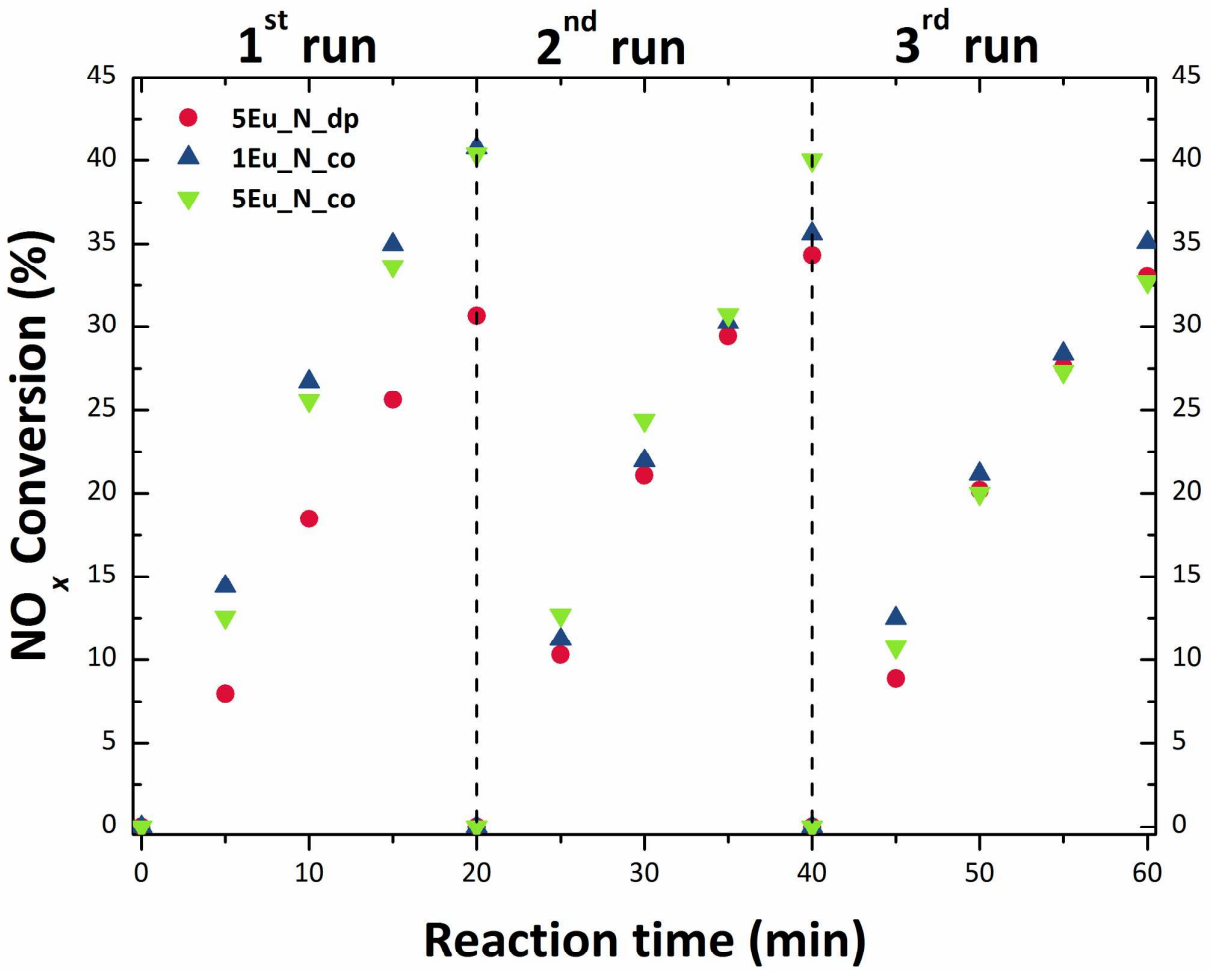

Fig. 8b

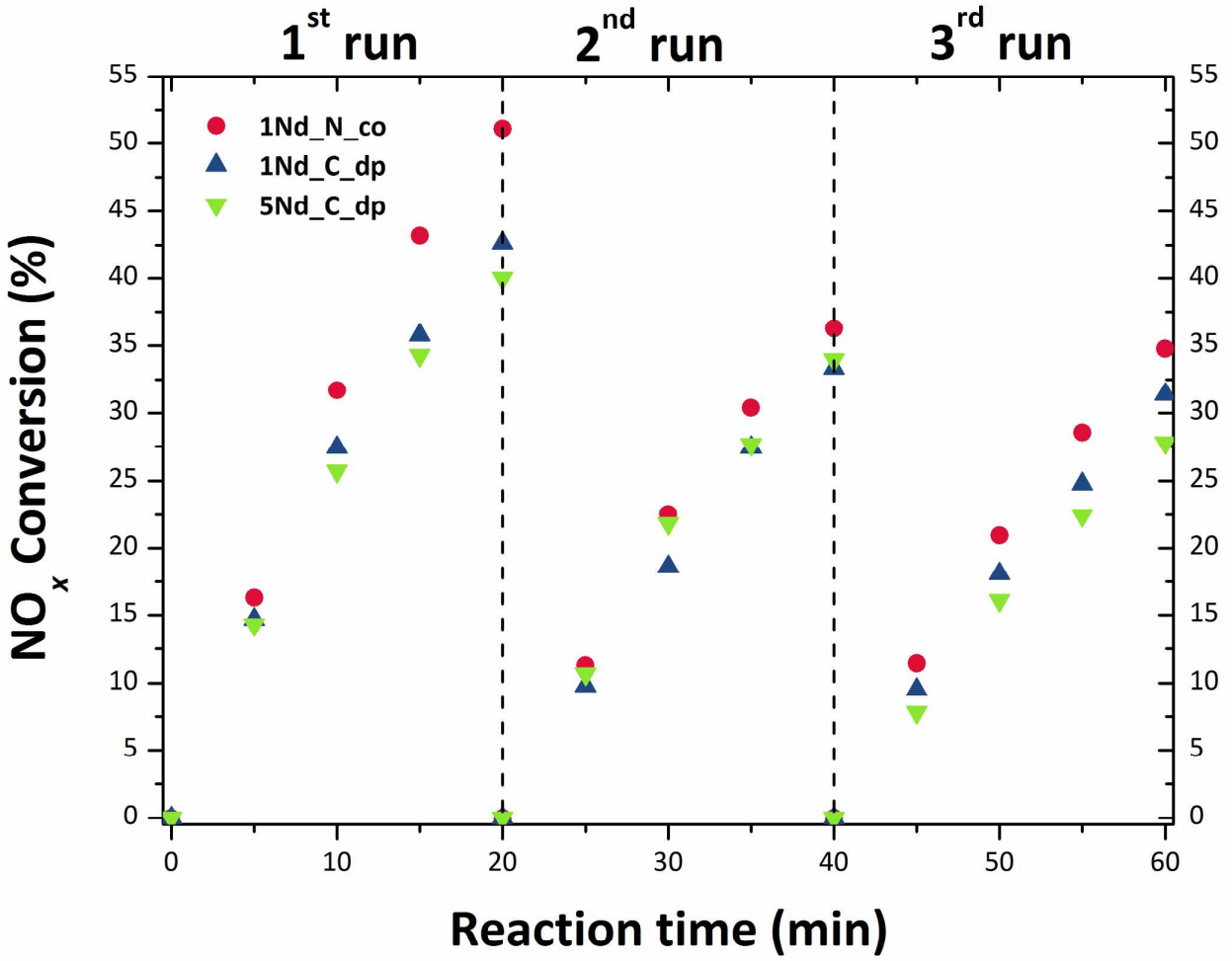

Fig. 8c

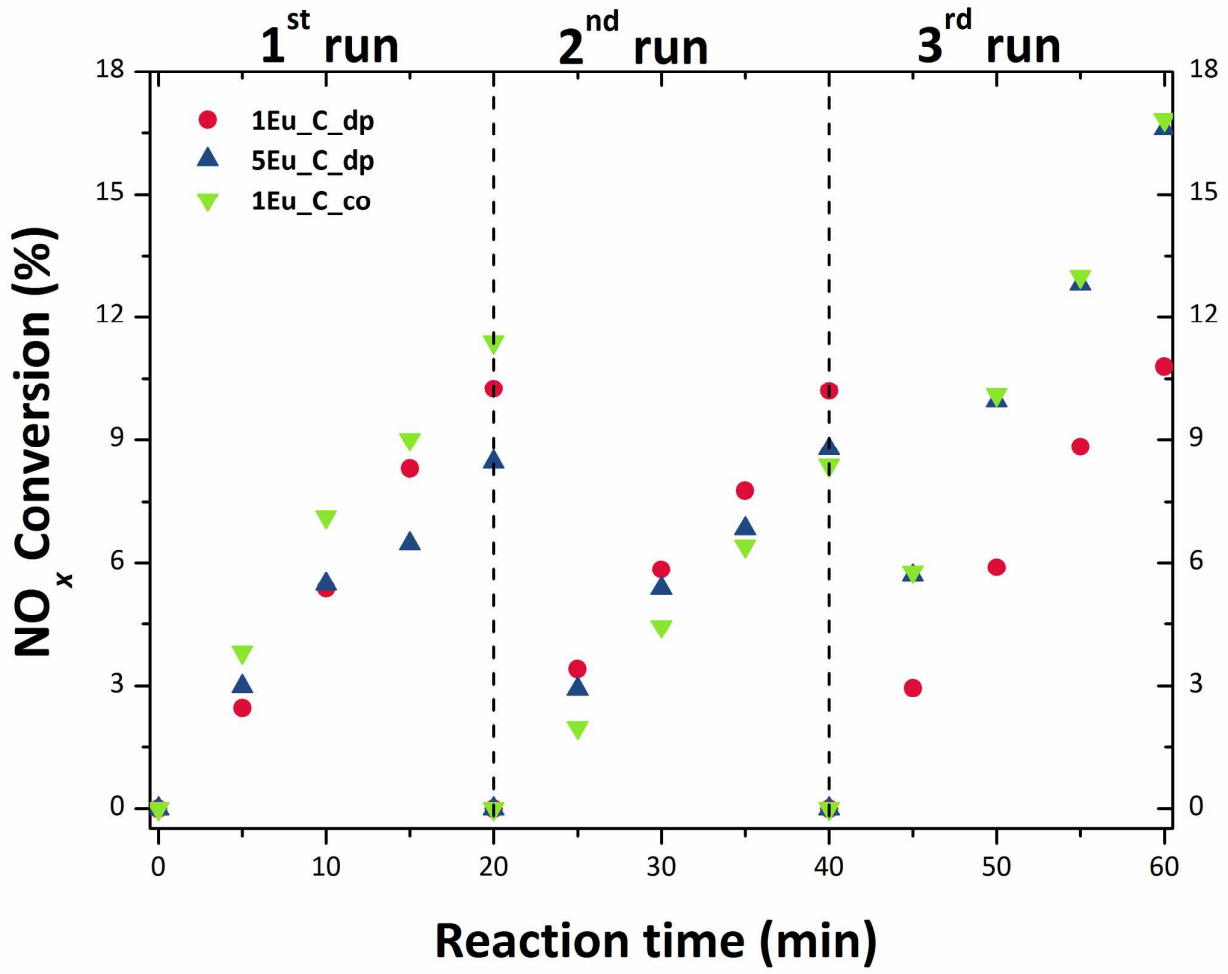

Fig. 8d

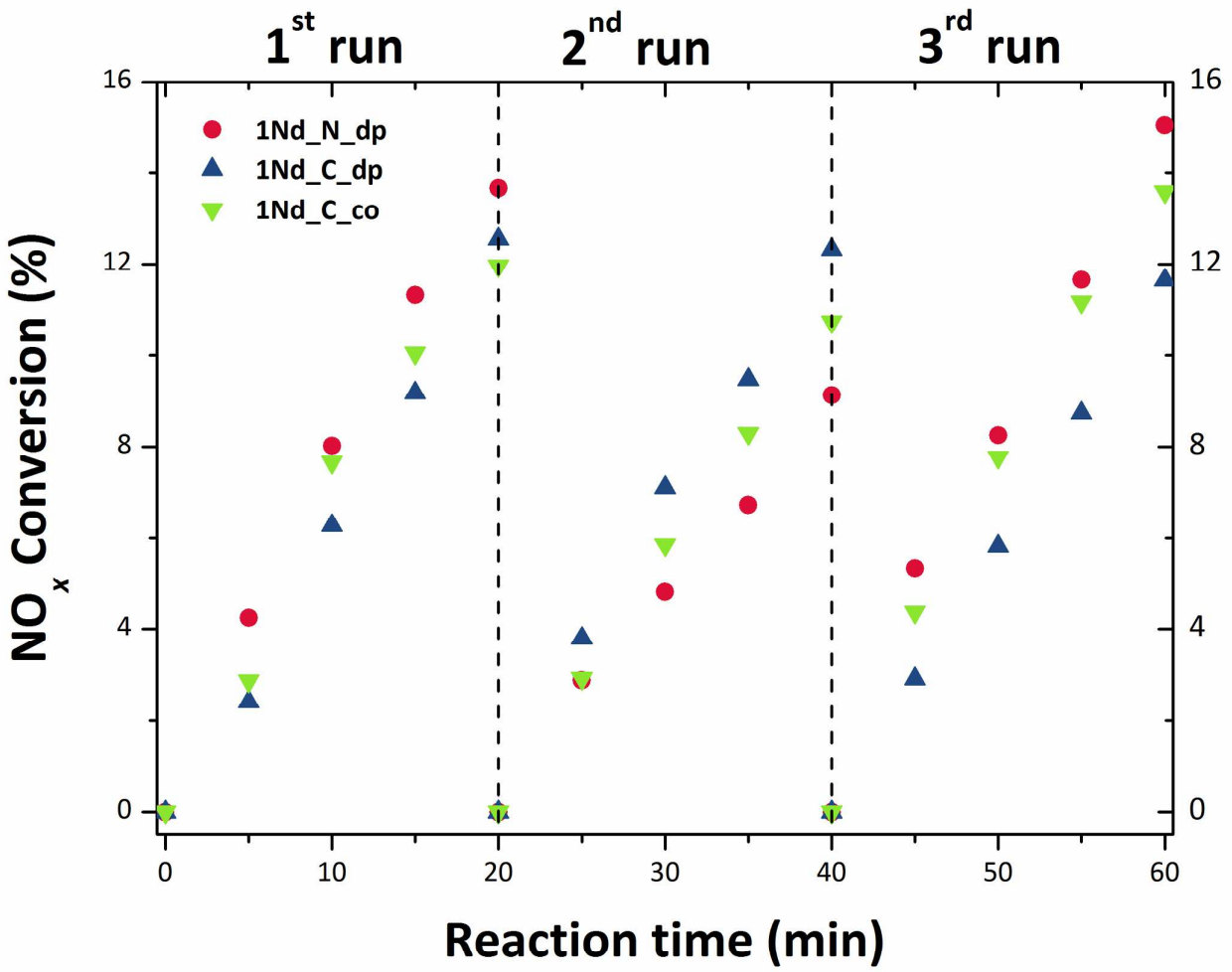

Tables

Table 1 − PCS number size distributions for RE-Ti sols. Columns show number average particle diameter, standard deviation of this, and the size range of particles detected, all in nm.

Sol	No. Av (nm)	SD (nm)	Size range (nm)
1%Eu_N_dp	31.79	10.22	18-80
5%Eu_N_dp	39.44	12.10	24-125
1%Eu_N_co	42.83	14.79	25-100
5%Eu_N_co	50.81	14.92	30-125
1%Eu_C_dp	14.60	3.45	10-30
5%Eu_C_dp	13.57	4.01	9-40
1%Eu_C_co	8.11	2.56	5-25
5%Eu_C_co	5.92	2.03	4-20
1%Nd_N_dp	5.17	1.14	4-12
5%Nd_N_dp	7.81	1.45	5-13
1%Nd_N_co	4.15	1.29	3-13
5%Nd_N_co	5.01	1.16	3-11
1%Nd_C_dp	3.53	1.02	2-11
5%Nd_C_dp	7.38	1.95	5-20
1%Nd_C_co	3.70	0.96	2-10
5%Nd_C_co	4.81	1.34	3-13

Table 2 – Semi-quantitative phase composition, from the Rietveld refinement of the X-ray data (not accounting for amorphous phase), for samples fired at 450 °C.

Sample	No. of variables	Agreement factors			Phase composition (wt%)		
		$R(_F^2)$ (%)	R_{wp} (%)	χ^2	anatase	rutile	brookite
TiO_2	20	6.05	6.27	2.37	42.9±0.2	49.1±0.2	8.0±1.1
1%Eu_N_dp	26	2.50	4.63	1.41	41.1±0.6	28.1±0.3	30.8±1.9
5%Eu_N_dp	20	1.54	4.31	1.36	34.3±0.6	6.3±0.3	59.4±1.1
1%Eu_N_co	25	1.72	4.76	1.46	30.3±0.6	29.9±0.2	39.9±1.8
5%Eu_N_co	20	1.74	4.49	1.40	37.4±0.6	14.5±0.3	48.0±1.3
1%Eu_C_dp	22	2.70	6.60	1.48	43.8±0.4	9.1±0.3	47.1±0.7
5%Eu_C_dp	20	3.02	4.46	1.46	42.1±0.5	5.2±0.4	52.7±0.9
1%Eu_C_co	22	2.53	4.69	1.49	44.3±0.5	17.1±0.2	38.5±1.4
5%Eu_C_co	22	1.63	4.26	1.30	50.4±0.5	10.7±0.3	38.9±1.5
1%Nd_N_dp	24	2.19	4.44	1.37	54.9±0.5	8.7±0.2	36.5±1.8
5%Nd_N_dp	21	1.10	4.63	1.43	43.3±0.5	6.1±0.3	50.6±1.5
1%Nd_N_co	20	2.53	4.50	1.39	52.1±0.3	11.8±0.2	36.1±0.8
5%Nd_N_co	20	1.75	4.71	1.54	45.5±0.5	7.7±0.3	46.9±1.8
1%Nd_C_dp	22	2.05	4.43	1.36	41.6±0.4	11.1±0.3	47.3±1.1
5%Nd_C_dp	20	2.00	4.44	1.39	42.8±0.5	7.0±0.3	50.2±1.0
1%Nd_C_co	20	2.40	4.55	1.40	48.6±0.3	9.8±0.3	41.6±0.8
5%Nd_C_co	20	1.65	4.40	1.26	33.7±0.6	9.3±0.3	57.0±1.2

Table 3 – Agreement factors and unit cell parameters of anatase, rutile and brookite, as calculated via WPPM modelling.

	Agreement Factors			Unit cell parameters									
				Anatase			Rutile			Brookite			
Sample	R_{wp} (%)	R_{exp} (%)	χ^2	$a = b$ (nm)	c (nm)	Volume (nm^3)	$a = b$ (nm)	c (nm)	Volume (nm^3)	a (nm)	b (nm)	c (nm)	Volume (nm^3)
TiO_2	3.56	1.61	2.21	0.3787(1)	0.9522(1)	0.137(1)	0.4595(1)	0.2959(1)	0.062(1)	0.5369(5)	0.9225(5)	0.5218(2)	0.258(1)
1%Eu_N_dp	2.85	1.48	1.92	0.3806(4)	0.9617(19)	0.139(1)	0.4598(1)	0.2959(1)	0.063(1)	0.5448(14)	0.9167(21)	0.5164(5)	0.258(1)
5%Eu_N_dp	1.94	1.38	1.41	0.3818(31)	0.9601(139)	0.140(4)	0.4601(3)	0.2960(2)	0.063(1)	0.5515(21)	0.9156(39)	0.5169(13)	0.261(3)
1%Eu_N_co	3.18	1.43	2.23	0.3807(12)	0.9589(15)	0.139(1)	0.4600(1)	0.2960(1)	0.063(1)	0.5427(10)	0.9216(20)	0.5172(5)	0.259(1)
5%Eu_N_co	2.40	1.37	1.75	0.3852(2)	0.9746(14)	0.145(1)	0.4604(2)	0.2959(2)	0.063(1)	0.5468(19)	0.9264(41)	0.5197(10)	0.263(3)
1%Eu_C_dp	4.40	1.49	2.96	0.3795(3)	0.9592(13)	0.138(1)	0.4604(2)	0.2960(1)	0.063(1)	0.5441(5)	0.9216(11)	0.5161(3)	0.259(1)
5%Eu_C_dp	1.95	1.50	1.30	0.3805(31)	0.9691(61)	0.140(3)	0.4627(5)	0.2974(4)	0.064(1)	0.5457(17)	0.9316(33)	0.5224(11)	0.266(2)
1%Eu_C_co	3.67	1.58	2.32	0.3836(21)	0.9626(22)	0.142(2)	0.4605(2)	0.2960(1)	0.063(1)	0.5425(7)	0.9271(12)	0.52301(4)	0.263(1)
5%Eu_C_co	2.18	1.51	1.45	0.3859(9)	0.9653(64)	0.144(2)	0.4681(7)	0.2989(4)	0.065(1)	0.5439(57)	0.9576(113)	0.5238(30)	0.273(8)
1%Nd_N_dp	5.02	1.61	3.12	0.3827(5)	0.9735(10)	0.143(1)	0.4598(1)	0.2959(1)	0.063(1)	0.5446(3)	0.9222(12)	0.5183(4)	0.260(1)
5%Nd_N_dp	2.81	1.63	1.73	0.3839(10)	0.9788(66)	0.144(2)	0.4643(8)	0.2973(4)	0.064(1)	0.5514(79)	0.9268(98)	0.5259(23)	0.269(8)
1%Nd_N_co	4.49	1.50	2.99	0.3828(4)	0.9744(13)	0.143(1)	0.4601(1)	0.2960(1)	0.063(1)	0.5444(4)	0.9269(11)	0.5175(3)	0.261(1)
5%Nd_N_co	2.82	1.57	1.80	0.3863(29)	0.9773(18)	0.146(3)	0.4618(3)	0.2968(3)	0.063(1)	0.5374(62)	0.9517(85)	0.5254(24)	0.269(7)
1%Nd_C_dp	4.21	1.89	2.23	0.3838(2)	0.9749(10)	0.144(1)	0.4634(2)	0.2973(2)	0.064(1)	0.5451(8)	0.9296(18)	0.5183(5)	0.263(1)
5%Nd_C_dp	2.78	2.03	1.37	0.3802(12)	0.9840(230)	0.142(4)	0.4631(10)	0.2968(8)	0.064(1)	0.5580(56)	0.9384(116)	0.5093(47)	0.267(9)
1%Nd_C_co	3.58	2.05	1.75	0.3825(12)	0.9701(22)	0.142(1)	0.4595(3)	0.2952(2)	0.062(1)	0.5442(6)	0.9194(20)	0.5178(8)	0.259(1)
5%Nd_C_co	2.98	1.84	1.62	0.3845(57)	0.9749(93)	0.144(6)	0.4638(5)	0.2968(5)	0.064(1)	0.5461(63)	0.9303(119)	0.5223(37)	0.265(8)

Table 4 – Position and full width at half maximum (FWHM) of Raman E_g mode of anatase in selected samples.

Sample	Anatase E_g mode (cm^{-1})	FWHM (cm^{-1})
TiO_2	145.3(1)	15.1(4)
1%Eu_N_dp	147.6(1)	20.1(7)
5%Eu_N_dp	150.6(2)	25.4(9)
1%Nd_N_co	146.6(1)	21.4(8)
5%Nd_C_dp	148.4(1)	25.2(7)

Table 5 − Mean crystalline domain size of anatase (ant), rutile (rt) and brookite (brk) – defined as the mean of the lognormal size distribution; maximum values of the lognormal size distribution – defined as the mode of the lognormal size distributions.

Sample	Mean crystalline domain size			Mode of the size distribution		
	$\langle D_{ant} \rangle$ (nm)	$\langle D_{rt} \rangle$ (nm)	$\langle D_{brk} \rangle$ (nm)	Ant (nm)	Rt (nm)	Brk (nm)
TiO_2	8.6±1.1	17.7±1.6	11.2±2.5	6.5±0.8	13.8±1.2	10.6±2.4
1%Eu_N_dp	5.6±0.7	12.5±1.8	6.5±0.8	5.0±0.6	10.0±1.4	6.1±0.7
5%Eu_N_dp	6.0±1.3	8.8±1.1	3.7±0.8	5.8±1.3	7.4±0.9	3.1±0.6
1%Eu_N_co	6.2±0.8	11.8±1.3	5.7±1.0	6.1±0.7	9.3±1.0	5.2±0.9
5%Eu_N_co	4.9±0.9	9.3±2.4	4.3±0.4	3.5±0.7	7.8±2.0	3.9±0.3
1%Eu_C_dp	6.3±1.7	11.1±3.7	7.0±0.8	5.7±1.6	9.5±3.2	6.4±0.7
5%Eu_C_dp	6.6±1.9	10.3±1.8	4.4±1.2	6.4±1.8	9.0±1.5	3.7±1.0
1%Eu_C_co	5.9±1.6	9.1±0.3	6.1±0.2	5.2±1.4	7.3±0.3	5.3±0.2
5%Eu_C_co	6.1±1.6	11.6±1.2	4.1±1.5	5.6±1.5	10.7±1.1	3.6±1.3
1%Nd_N_dp	5.5±1.0	13.2±1.2	4.3±0.3	5.2±0.9	10.8±1.0	3.4±0.2
5%Nd_N_dp	6.5±0.5	12.3±1.7	4.1±0.3	6.1±0.5	11.8±1.6	3.8±0.3
1%Nd_N_co	6.8±1.3	12.0±0.7	5.7±0.3	6.7±1.3	9.5±0.6	5.0±0.2
5%Nd_N_co	5.8±0.1	9.1±0.7	3.8±0.2	5.5±0.1	8.0±0.6	3.3±0.2
1%Nd_C_dp	6.0±0.3	10.5±0.7	6.9±0.3	5.4±0.3	9.3±0.6	6.1±0.3
5%Nd_C_dp	4.9±0.3	7.2±1.2	6.7±0.5	4.4±0.3	6.3±1.0	6.5±0.4
1%Nd_C_co	5.1±1.9	12.5±1.1	6.8±0.2	4.8±1.8	11.4±1.0	6.4±0.2
5%Nd_C_co	5.1±1.5	6.6±0.8	6.6±0.6	4.9±1.4	5.2±0.7	6.5±0.6

Table 6 – Optical energy band gap (E_g), as calculated *via* the differential reflectance method.

	E_g (eV)		
Sample	anatase	rutile	brookite
TiO_2	–	3.06±0.01	–
1%Eu_N_dp	3.17±0.02	3.06±0.01	–
5%Eu_N_dp	3.28±0.01	3.10±0.01	3.40±0.02
1%Eu_N_co	–	3.06±0.01	–
5%Eu_N_co	3.29±0.01	3.08±0.01	3.41±0.02
1%Eu_C_dp	–	3.06±0.01	–
5%Eu_C_dp	–	3.11±0.01	–
1%Eu_C_co	–	3.08±0.01	–
5%Eu_C_co	–	3.09±0.01	–
1%Nd_N_dp	3.25±0.01	3.08±0.01	–
5%Nd_N_dp	3.31±0.02	3.08±0.01	–
1%Nd_N_co	3.29±0.01	3.08±0.01	3.39±0.02
5%Nd_N_co	3.24±0.06	3.08±0.01	3.40±0.02
1%Nd_C_dp	–	3.10±0.01	–
5%Nd_C_dp	3.21±0.02	3.11±0.01	3.44±0.02
1%Nd_C_co	–	3.10±0.01	–
5%Nd_C_co	3.32±0.02	3.10±0.01	3.46±0.02

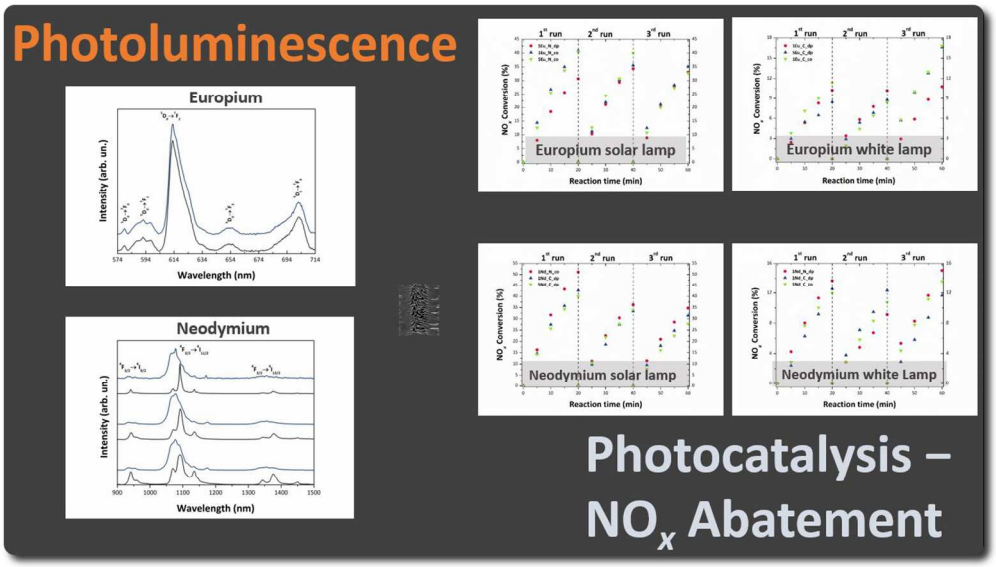

118x67mm (300 x 300 DPI)